Heusler compounds as thermoelectric materials

Dissertation
zur Erlangung des Grades
"Doktor der Naturwissenschaften"
am Fachbereich Chemie, Pharmazie und Geowissenschaften
der Johannes Gutenberg-Universität Mainz

vorgelegt von
Joachim Barth
geboren in Kaiserslautern

Mainz, 2009

”Ob man glaubt, man könne, oder glaubt, man könne nicht - man hat recht.”

Henry Ford

Hiermit versichere ich, dass ich die vorliegende Dissertation selbständig verfasst und keine anderen als die angegebenen Hilfsmittel benutzt habe. Alle der Literatur entnommenen Stellen sind als solche gekennzeichnet.

Mainz, Juli 2009

Contents

1 Introduction

1.1 Motivation

The world's increasing demand for energy and the global climate change are of utmost political and economical importance [1]. Ways to improve the sustainability of our electricity base and the reduction of the need for fossil fuels have to be found. One way is the scavenging of waste heat with thermoelectric generators [2]. The waste heat from industrial processes and automotive exhaust gases are formidable targets for the conversion of heat into electricity. The use of thermoelectric generators as sources for electrical power is very convenient because they are solid-state devices with no moving parts, they are silent, and of high durability. Advances in the field of thermoelectrics will enable the production of economic thermoelectric generators and the construction of efficient cooling devices. In Figure 1.1 the schematic view of a thermoelectric generator is displayed. The thermal gradient leads to a voltage difference. It has to be noted that the current flow marked by the arrows is from + to -. The flow of the electrons is opposite to that. The quality of a thermoelectric material is given by its figure of merit at a certain temperature [3]. High operating temperatures of the devices are favourable because the efficiency is a product of the Carnot cycle and the figure of merit and therefore increases with high temperature differences. Thermoelectric materials with high figures of merit for various working temperatures have been found for several material classes. Among the material classes with high potential are: classic semiconductors, bismuth tellurides [4], SiGe [5] and especially

- compounds of the AlLiSi structure type, like compounds based on TiNiSn, which are known to have a $ZT \approx 1.5$ at 800 K [6]
- filled scutterudite compounds, like $CeFe_4Sb_{12}$, Yb_xCoSb_3 with a ZT≈1.2 at 700 K [7, 8]
- metal oxides Na_xCoO_2 [9]
- semiconducting clathrates, e.g. $Sr_8Ga_{16}Ge_{30}$ with a ZT≈1 at 700 K [10]
- complex Bi chalcogenides with a ZT≈0.8 at 225 K [11]
- cubic AgPbSbTe bulk compounds with nanocrystalline embeddings with ZT≈2.2 at 800 K [12]

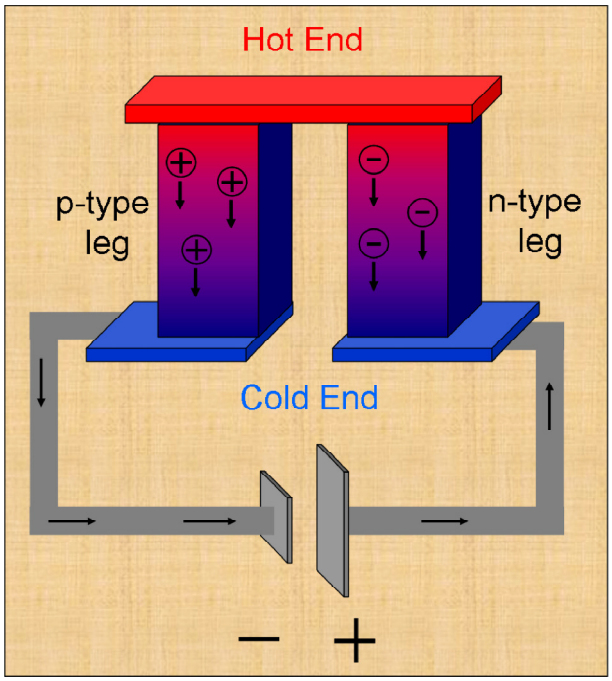

Figure 1.1: Schematic drawing of a thermoelectric generator

Significant improvements of the figure of merit compared to the bulk materials have been achieved by thin film materials like Bi_2Te_3/Sb_2Te_3 [13] and $PbSe_{0.98}Te_{0.02}/PbTe$ [7]. Bi_2Te_3/Sb_2Te_3 superstructures define the state of the art with a ZT value of 2.4 at room temperature. For industrial purposes huge amounts of material are needed. Therefore, the search for new bulk materials with similar ZT values is of highest priority. One structure type that meets the prerequisites for bulk materials is the structure type AlLiSi which is sometimes also called $C1_b$ or Half Heusler. Usually those are semiconductors with a small energy gap between 0.1 and 1.0 eV [8, 14, 15]. More than 250 compounds of this structure type are known. Heusler compounds are known to be very versatile, mainly due to their special magnetic and electric properties. Especially the carrier density and the type of conduction mechanism, namely hole or electron, can be easily modified. Only few investigations have been carried out in this field of research. In the focus of recent investigations were the ternary, intermetallic compounds of the general formula XNiSn(X=Ti, Zr, Hf) which show figures of merit up to 1.5 at 800 K [16]. One of the major drawbacks of the Heusler compounds and their structural derivative the $C1_b$ compounds is their high thermal conductivity compared to the other state of art materials. Therefore, several attempts have been ventured to reduce the thermal conductivity. Hohl and coworkers [17] have substituted the Ti position of TiNiSn with Zr and Hf. This resulted in a reduction of the thermal conductivity by two thirds in a large temperature range due to the increased phonon scattering [17]. With

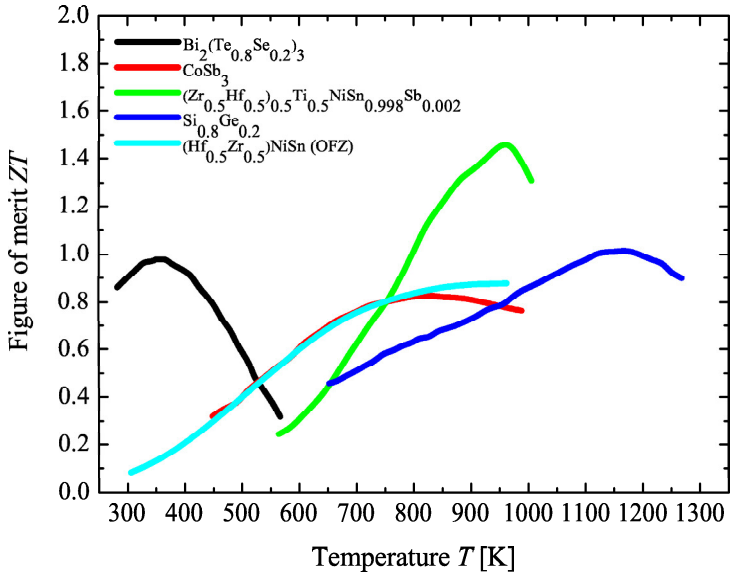

Figure 1.2: Displayed are the temperature dependent ZT values of selected Heusler compounds and state of the art materials.

the additional substitution of Sn by Sb the thermal conductivity is reduced even further and the electrical conductivity is increased at the same time [18]. The figure of merit for several state of the art materials and for two Heusler compounds is displayed in Figure 1.2. The highest figure of merit that has been achieved with Heusler compounds so far is 1.5 at 693 K [6] for the compound $Ti_{0.5}(Zr_{0.5}Hf_{0.5})_{0.5}NiSn_{0.998}Sb_{0.002}$. As one can see the ZT values for Heusler compounds [6, 19] are comparable to bulk state of the art materials or even exceed their performance. This and their other before mentioned benefits make their potential as materials for thermoelectric generators apparent. Further investigations of the Heusler compounds and their thermoelectric properties are necessary to explore their value as materials for thermoelectric applications. This thesis is contributed to the exploration of the structural and thermoelectrical properties of the Heusler compounds.

1.2 Structures

In this work mainly two structure types were studied. The first one is the $C1_b$ structure, also known as Half Heusler structure. The second one is the $L2_1$ structure also known as Heusler structure [20, 21]. Both are intermetallic compounds with the formula XYZ for $C1_b$ and X_2YZ [22] for $L2_1$ (X, Y=transition metals, Z=main-group element). From the viewpoint of electronic structures the most appropriate description for the $C1_b$

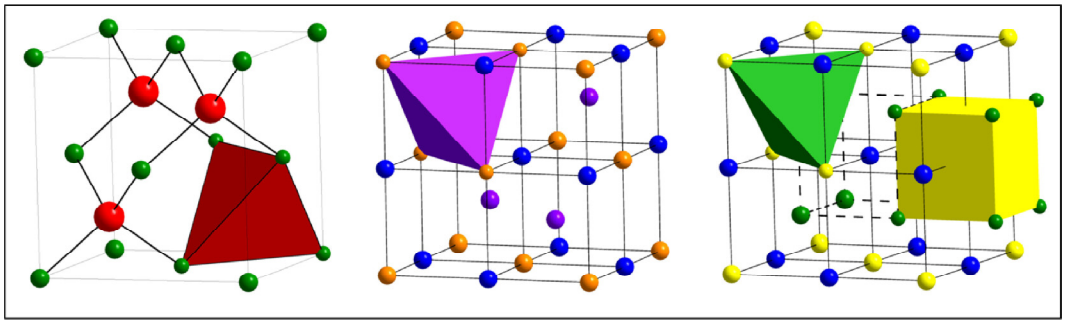

Figure 1.3: From the left to the right the unit cell for the zinc-blende($B3$), Half Heusler($C1_b$), and Heusler($L2_1$) structure types are displayed.

structure is a zinc-blende YZ lattice stuffed with X atoms, as it is shown in Figure 1.3. Another and more common description is that Half Heusler compounds exhibit the cubic AlLiSi($C1_b$) crystal structure consisting of 3 filled and 1 vacant interpenetrating fcc sublattices. The third fcc structure is shifted by 1/4 of the unit cell from the body diagonal of the rock salt structure [23, 24]. In the Heusler alloys two sublattices occupy X and thus there is no vacant sublattice. However, one should note that the additional X atom fills the remaining tetrahedral vacancy in the XYZ. This changes the symmetry of the crystal structure, because the X atoms occupy sites with T_d symmetry and the Y and Z atoms occupy sites with O_h symmetry.

1.3 Figure of merit

The efficiency for the energy conversion η in thermoelectric modules is determined by

$$\eta = \frac{T_H - T_C}{T_H} \frac{\sqrt{1+ZT}-1}{\sqrt{1+ZT}+\frac{T_c}{T_H}}, \tag{1.1}$$

with T_H being the high temperature, T_C the low temperature, Z is the figure of merit, a material dependent value, and T is the absolute temperature. The first part of the product represents the Carnot process and gives a general limit for the efficiency of thermodynamic processes. The second part of the product is mainly dependent on the figure of merit Z. In Figure 1.4 the efficiency of a thermoelectric module versus the temperature difference for several values of the figure of merit is displayed. The higher the figure of merit and the higher the temperature difference is, the higher is the efficiency. Therefore it is needed to find not only a high value of Z but materials that are stable at the appropriate temperature as well. The dimensionless figure of merit [3]

$$ZT = \frac{S^2}{\rho \cdot \kappa} \cdot T \tag{1.2}$$

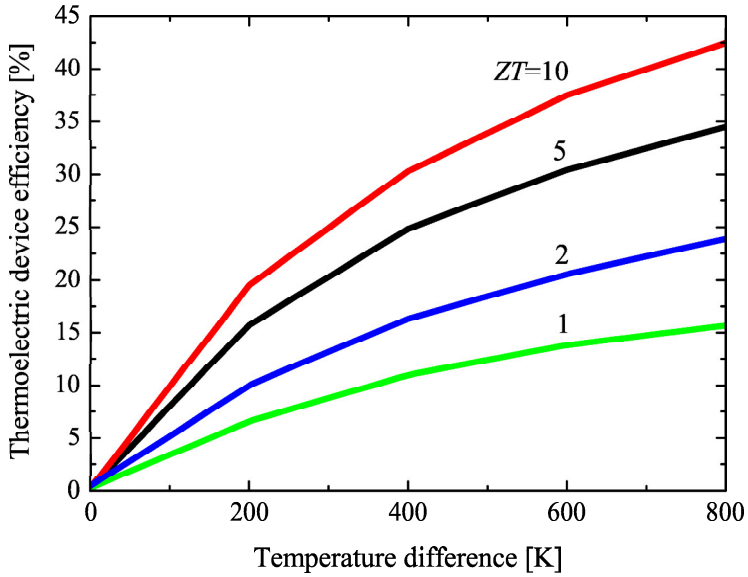

Figure 1.4: Thermoelectric power generation efficiency [25]

is composed of the square of the Seebeck coefficient S^2, the electrical resistivity ρ, the thermal conductivity κ and the absolute temperature T.

The Seebeck coefficient and electrical resistivity depend strongly on the Fermi level [26] which depends on the carrier concentration, the carrier's effective mass, and the temperature. Considering a single band with a parabolic density of states distribution using classical statistics the Seebeck coefficient [27] can be expressed as

$$S = \pm k/e(5/2 + s - \xi). \tag{1.3}$$

The $\pm$ refers to the contribution of electrons and holes, respectively. $\xi = (E_F/kT)$ is the reduced Fermi energy, k is the Boltzmann's constant, T the absolute temperature, s refers to the scattering parameter and it is assumed that the carrier relaxation time can be expressed in terms of the carrier energy in a simple way, i.e. τ is proportional to E. The electrical conductivity is given by

$$\sigma = ne\mu \tag{1.4}$$

where μ is the carrier mobility in the low carrier concentration limit. Alternatively to the electrical conductivity the term of electrical resistivity is used. The electrical resistivity ρ is given by

$$\rho = 1/\sigma. \tag{1.5}$$

The carrier concentration is related to the reduced Fermi energy by the equation

$$n = 2(2\pi m^* kT/h^2)^{3/2} exp^{\xi}. \tag{1.6}$$

For the description of the thermal conductivity κ, the term

$$\kappa = \kappa_l + \kappa_e \tag{1.7}$$

is used. κ_l is the lattice thermal conductivity and κ_e is the electronic thermal conductivity. The thermal conductivity is affected by ξ only through the electronic contribution κ_e. κ_e can be expressed using the equation

$$\kappa_e = L_0(k/e)^2 \sigma T, \tag{1.8}$$

with L_0 being the Lorenz factor. With the introduction of the parameters F and G

$$F = \frac{\mu}{\kappa_l} \left(\frac{m^*}{m} \right)^{3/2} \tag{1.9}$$

$$G = (2\pi m kT/h^2)^{3/2} \tag{1.10}$$

the figure of merit can be expressed as

$$Z = \frac{(5/2 + s - \xi)^2}{(2\frac{k^2}{e} \cdot F \cdot G \cdot exp\xi)^{-1} + (5/2 + s)T}. \tag{1.11}$$

For a more differentiated view the figure of merit is often decomposed into the numerator and the denominator. The numerator is then called Power factor(PF). With this step the electronic properties can be separated from the thermal conductivity. This approach is only viable for materials with a phonon dominated thermal conductivity.

$$ZT = \frac{PF}{\kappa} \cdot T \Rightarrow PF = S^2 \cdot \sigma \tag{1.12}$$

Within this approach the Power factor can be optimized for a certain electron concentration. This is shown in Figure 1.5. The Seebeck coefficient (left axis) and the electrical conductivity (right axis) are plotted versus the carrier concentration. The Seebeck coefficient is high for low carrier concentrations and declining for higher carrier concentrations. Vice versa is true for the electrical conductivity. The opposing behaviour of the two factors results in a maximum for the Power factor for a carrier concentration of about $10^{20}\mathrm{m}^{-3}$. This maximum corresponds to heavily doped semiconductors or semimetals. $C1_b$ compounds with 18 valence electrons are often semiconductors or half metals and are therefore well suited for the use as thermoelectric materials. Similar

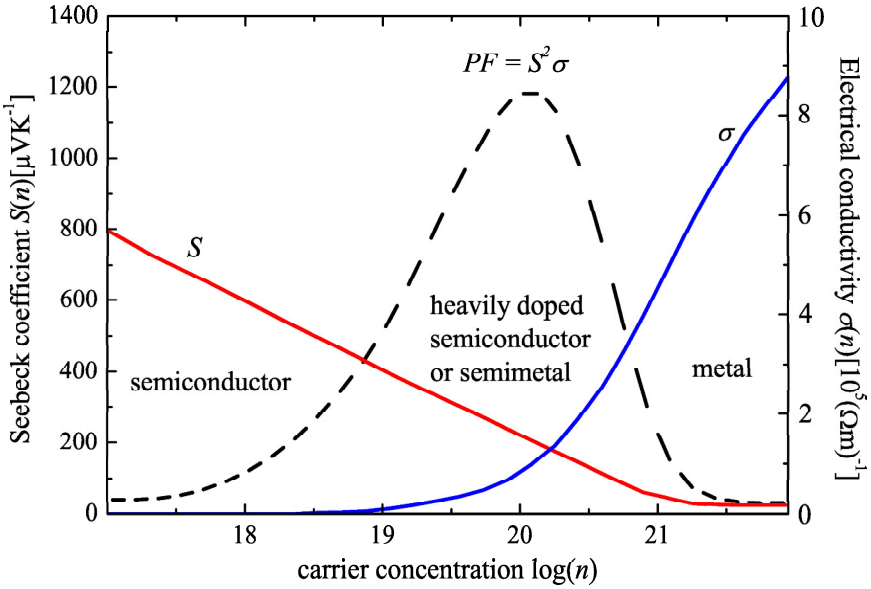

Figure 1.5: Displayed are the Seebeck coefficient and the electrical conductivity versus the carrier concentration. The dotted line represents the power factor.

conclusions can be drawn for Heusler compounds with 24 valence electrons, although these usually are small gap semiconductors or half metals [28].

1.4 Investigations of this thesis

The focus of this thesis is the systematic investigation of the figure of merit for $C1_b$ and $L2_1$ compounds. The compounds were synthesized and their thermoelectric properties were determined. Various approaches were used to change the thermoelectric properties. In chapter 3 Co is substituted by equal parts of Ni and Fe in the solid solution $TiCo_{1-x}(Ni_{0.5}Fe_{0.5})_xSb$. Aim of the substitution is the reduction of the phononic part of the thermal conductivity by the introduction of additional mass fluctuation scattering. The series is supposed to be semiconducting, but the density of states at the Fermi energy should change. This affects the electronic properties. Furthermore, the stability of the compound is investigated. In chapter 4 the solid solution $TiNi_{1-x}Co_xSn_{1-x}Sb_x$ between TiCoSb and TiNiSn is investigated. Co is substituted by Ni and Sb is substituted with Sn. The whole series has 18 valence electrons(VE) and therefore is supposed to be semiconducting. The influence of atomic disorder on the properties is discussed. In chapter 5 the Li containing compounds LiAlSi, LiAlGe, and LiGaSi referred to as LiYZ are investigated. Li containing compounds with porous structures are supposed to have small thermal conductivities. The small thermal conductivity is caused by the

high phonon scattering of the rattling Li ions. In chapter 6 several compounds based on TiCoSb were investigated. The according series are $TiCo_{1+x}Sb$, $TiCo_{1-x}Cu_xSb$, and $TiCoSb_{1-x}Bi_x$. For $TiCo_{1\pm x}Sb$ Co was removed from the compound or inserted into the vacant sublattice. The change of the thermoelectric properties was determined. In the solid solution $TiCo_{1-x}Cu_xSb$ Co was substituted by Cu. By this substitution the carrier concentration changes and the electronic properties are influenced. In this way the Power factor can be optimized. In the solid solution $TiCoSb_{1-x}Bi_x$ Sb is substituted by Bi. The higher mass of Bi is supposed to reduce the thermal conductivity. In chapter 7 the series Co_2TiZ, with Z =Si, Ge and Sn was investigated. The compounds are supposed to be half metallic ferromagnets. This material class has not been investigated as a thermoelectric material before. Band structure calculations and valence band spectroscopy were performed and the magnetic properties were determined. The chapter is focused on the ferromagnetic to paramagnetic transition occurring at the Curie temperature and its influence on the electronic structure.

The results of the investigations help to explain the thermoelectric and structural properties of $L2_1$ and $C1_b$ compounds. With this knowledge the efficiency of thermoelectric devices can be improved and more efficient devices can be designed.

2 Experimental Details

All polycristalline samples were prepared by arc melting of stoichiometric amounts of the constituents in an argon atmosphere at 10 ^{4} mbar. Care was taken to avoid oxygen contamination. This was ensured by evaporating Ti inside of the vacuum chamber before melting the compound as well as by additional purification of the process gas. The samples were not annealed, unless stated otherwise.

The crystallographic structure was investigated by X-ray powder diffraction(XPD) using excitation by Mo K_α (Bruker, AXS D8) in reflection geometry or Cu K_α radiation (Bruker, D500) in transmission geometry in a $\theta - \theta$ scanning mode. The samples were crushed by hand using a mortar. The resulting powder was used for the XRD investigations.

Differential scanning calorimetry (DSC) measurements (NETZSCH, STA 429) were performed to detect phase transitions. The differential thermal analysis(DTA) and the thermal gravimetry(TG) were simultaneously performed with the thermal analyzer NETZSCH STA 409. The measurements were performed in a steady Ar flow and a heating rate of 10 K/min. For the measurements pieces of 80 mg-120 mg were used.

For the inspection of the surface an EDX-Detection system (Surface Concept GmbH) was used that is additionally equipped with a scanning electron microscope (Jeol JSM-6400). The samples were measured in a vacuum of 3×10^{-6} mbar. An acceleration voltage of 20 kV was applied and an inspection angle of 35° was set up. For the correction the ZAF method was applied. For the image acquisition the Digital Image Processing System(DIPS) and for the quantitative chemical analysis the program WINEDS 4.0 were used. For the chemical analysis the whole field of view is used unless stated otherwise. The measurements were performed by Andrei Hloskovskyy and Peter Klaer.

The measurements of the Seebeck coefficient, thermal conductivity, and resistivity were carried out with a Physical Property Measurement System (Model 6000 Quantum Design, with the options P400, P600, and P640) from 2 K to 400 K. The bars have been contacted by copper stripes, that were wrapped around the sample to homogenize the current passing through. Additionally the stripes were glued to the sample with a silver epoxy paste to improve the contact. Before contacting the samples were polished to remove oxide layers which may have formed between the synthesis and the measurement. The sample chamber was flooded with Argon and afterwards evacuated. The thermoelectric properties were measured at a pressure of about 1.2×10^{4} mbar by a standard four point ac method. An additional correction term for the heat loss at the heating shoes was introduced and applied to the thermal conductivity data as it was

suggested by Müller, Stiewe, Rowe and Williams [29] and Quantum Design [30]. As a test measurement a Ni sample provided by Quantum Design was measured to verify if the PPMS is working within the given parameters by the manufacturer. The measured values Ni_{exp} and the values given by Quantum Design Ni_{QD} are displayed in Figure 2.1. The measured data is consistent with the data provided by the manufacturer. For temperatures higher than 200 K a correction term for the thermal conductivity has to be introduced. The thermal conductivity is given by the measured thermal conductance multiplied by a geometry factor. The thermal conductance is determined as

$$K = \frac{(I^2R - P_{Rad})}{\Delta T - K_{shoes}}, \tag{2.1}$$

with I^2R being the power dissipated in the heater resistor.

$$K_{shoes} = aT + bT^2 + cT^3 \tag{2.2}$$

is the standard estimate of the thermal conductance of the shoe assemblies with a, b and c being constants, and

$$P_{Rad} = \sigma_T \times (S/2) \times \epsilon \times (T_{hot}^4 - T_{cold}^4) \tag{2.3}$$

the radiation from the sample. S is the total sample surface area, ϵ is the infrared emissivity of the radiating surface, T_{hot}/T_{cold} are the average temperatures of the hot and cold thermometers during the measurement and $\sigma_T = 5.67 \times 10^{-8} \frac{W}{m^2K^4}$. The factor of 1/2 is due to the approximation that only one half of the sample surface is radiating at the hot temperature whilst the other half is at the cold temperature. The largest error is inflicted by the term cT^3 of the radiation loss of the shoes. At higher temperatures where the cT^3 term dominates a correction factor has to be introduced to eliminate the resulting tail in the measurements.

The electrical conductivity and the Seebeck coefficient in the high temperature range were determined using the RZ2001i unit of Ozawa Science, Japan. The temperature range of the measurements are given in the chapters, respectively. Both parameters were recorded simultaneously as a function of temperature in Ar-atmosphere. The Seebeck coefficient was measured by a steady-state method and the electrical conductivity by the DC four-point method. The measurements of the electronic properties were carried out in Switzerland at the Eidgenössische Material Prüfungsanstalt(EMPA) by Andrey Shkabko and Rosa Roberts under the supervision of Anke Weidenkaff. The magnetic properties were investigated by a super conducting quantum interference device (SQUID, Quantum Design MPMS-XL-5) using nearly punctual pieces with approximate weights of 8 mg. The SQUID measurements and their interpretation were

performed by Benjamin Balke.

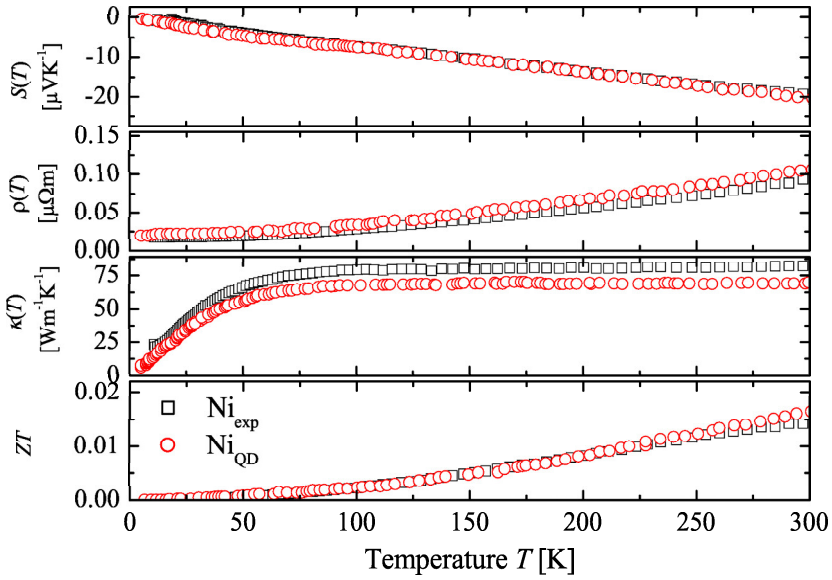

Figure 2.1: Thermoelectric properties of a Ni standard sample. Shown are the measured thermoelectric properties of the standard Ni sample, that is provided by the manufacturer. Part (a) shows the Seebeck coefficient $S(T)$, (b) the resistivity $\rho(T)$, (c) the thermal conductivity $\kappa(T)$, and (d) the dimensionless figure of merit ZT.

For the HArd X-ray PhotoEmission Spectroscopy (HAXPES) investigation, the sample bars were cleaved in situ. This assures that the samples are free of oxygen contaminations. The HAXPES experiments were performed at the beamline BL15XU of SPring-8 (Japan). The photon energy was fixed at 5.94677 keV using a double crystal monochromator and a Si(333) post monochromator. The photo emitted electrons were analyzed for their kinetic energy and detected by means of a hemispherical analyzer (Scienta). The overall energy resolution (monochromator plus analyzer) was set to 250 meV, as verified by spectra of the Au valence band at the Fermi energy (ϵ_F). The angle between the electron spectrometer and photon propagation is fixed at 90°. The photons are p-polarized, that is, the electric field vector is in the plane of incidence and always pointing in the direction of the electron detector. A near normal emission ($\theta = 8°$) detection angle was used. This corresponds to an angle of incidence of $\alpha = 90° - \theta = 82°$. (Note that the angles are not well defined for the cleaved bulk samples due to surface roughness.)

The electronic band structure and the electronic properties were calculated using the Wien2K and BoltzTrap codes. The calculations were performed by Gerhard H. Fecher,

details are given in chapter 6.

3 Thermoelectrical and structural properties of $TiCo_x(Ni_{0.5}Fe_{0.5})_{1-x}Sb$

3.1 Introduction

A very promising material class in the field of thermoelectric materials are compounds crystallizing in the structure type AlLiSi. Several compounds showing high ZT values have been found in this structure type. A well investigated compound of this material class is TiCoSb [31, 32]. Calculations predict an energy gap of 0.95eV at the Fermi energy which indicates the maximum figure of merit to be in the high temperature range [33, 34]. The optimum band gap E_{Gap} of a thermoelectric material and its resulting optimized operating temperature T can be estimated by

$$E_{Gap} = nk_BT, \tag{3.1}$$

with $n = 6 - 10$, k_B is the Boltzmann constant [35, 36, 37]. n depends strongly on the scattering mechanism and whether it is of parabolic or non parabolic nature. The resulting optimized operating temperature is between 1103 K and 1838 K for TiCoSb. Therefore, TiCoSb is supposed to be suitable for a high temperature application. However, it has to be taken into account that disorder reduces the gap and consequentially the optimized operating temperature. A high operating temperature is desirable because it enhances the thermoelectric conversion efficiency. The precondition for a high working temperature is the chemical stability. A major aspect influencing the chemical stability is the homogeneous and stoichiometric composition of a compound. The synthesis of stoichiometric and homogeneous TiCoSb is challenging, due to the evaporation of Sb during the synthesis [38, 39]. Small amounts of disorder and nonstoichiometric amounts of Sb change the electronic band structure significantly [34]. The loss of Sb during the arc melting can not be monitored by standard x-ray diffraction (XRD) because it is below its detection range. Resistivity measurements yield a metal to semiconductor transition in the low temperature range that indicates a non stoichiometric composition. It has been shown that annealing does not improve the thermoelectric properties [38]. The loss of Sb during synthesis causes several problems, e.g. fast degradation during use, difficult reproducibility, and an automatic doping. To stabilize the compound Co was substituted by equal amounts of Ni and Fe. The compound $TiNi_{0.5}Fe_{0.5}Sb$ is well known and characterized [40]. Within this approach the amount of valence electrons is not changed and the semiconducting properties should be maintained [15]. The solid solution $TiCo_x(Ni_{0.5}Fe_{0.5})_{1-x}Sb$ ($0 \leq x \leq 1$) was synthesized

and the thermoelectric properties were measured.

3.2 Results and Discussion

3.2.1 Structural Properties

To investigate the structural properties X-ray diffraction measurements were performed on the compounds. As an example the XRD pattern for $TiCo_{0.8}Ni_{0.1}Fe_{0.1}Sb$ is shown in Figure 3.1. A Rietveld refinement was performed on the pattern with Ti at the 4a Wyckoff position, Sb at the 4b position, Co, Ni, and Fe at the 4c position, and an assumed empty 4d position. For the refinement the first three indexed reflexes were used. The refinement yielded the best pattern R-Factors for an assumed antisite disorder of 5% between the Sb at the 4b position and the Co at the 4c position. An additional occupation of the 4d sublattice by excess Sb increases the R value of the refinement with increasing occupation of the 4d position. Therefore, it is assumed that the 4d sublattice is vacant and not filled with excess Sb. All samples show the $C1_b$ structure. A refinement of the powder pattern for TiCoSb yielded a lattice parameter of 5.879 Å. This is in agreement with the values found in literature of 5.884 Å [41] and 5.979 Å [42]. For the investigation of the change of the lattice parameter the compound $TiCo_{0.2}Ni_{0.4}Fe_{0.4}Sb$ was synthesized in addition to the existing solid solution. The change of the lattice parameter is displayed in the inset of Figure 3.1. A linear fit was applied to prove whether $a(x)$ follows Vegard's law [43]. The equation resulting from the linear fit is $a(x)$=-0.032x+5.911. It has to be noted, that with a decreasing Co content the lattice parameter is increasing. The averaged size of Ni and Fe are not equal to the one of Co in this solid solution.

As a further indication of the phase purity of the samples the resistivity measurements can be taken into account. Pure, wide band gap semiconductors should show a resistivity behaviour like it is displayed in Figure 3.2 for the measurement of TiCoSb*[34]. The resistivity behavior for unannealed TiCoSb is displayed as $TiCoSb_{imp}$ in the graph. It is assumed that the reduction of the resistivity and the metal to semiconductor transition are caused by impurities of Sb. The impurities arise during the synthesis in the arcmelting furnace, where Sb is partially evaporating. If the Co in TiCoSb is substituted by equal parts of Ni and Fe the evaporation is strongly reduced. This results in a diminishing of the metal to semiconductor transition and purely semiconducting behaviour. This is true for even very small amounts of substitution like it is shown for $TiCo_{0.98}Ni_{0.01}Fe_{0.01}Sb$. The resistivity reaches a maximum for $TiCo_{0.95}Ni_{0.025}Fe_{0.025}Sb$. For higher substitution levels the resistivity is decreasing again as shown in Figure 3.3. A small amount of impurity is detected for x=0 in the XRD pattern. Two different phases were identified. One is $TiSb_2$ and the other is Kamacite (Ni;Fe). An explanation

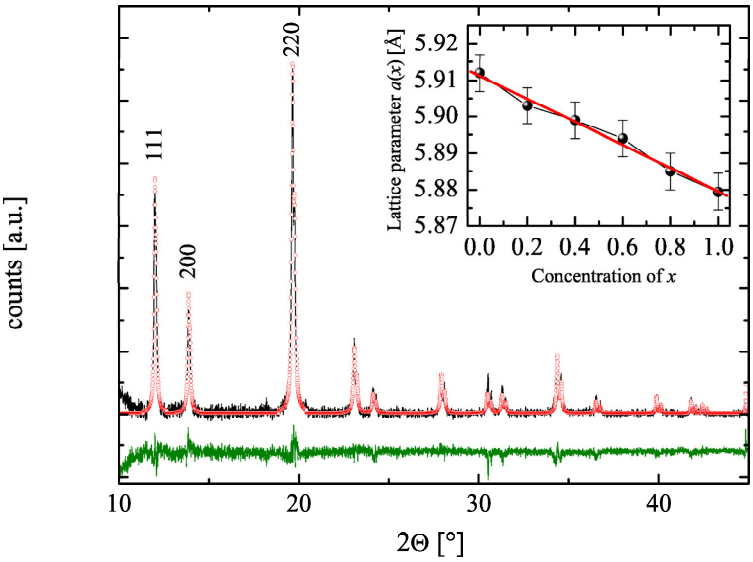

Figure 3.1: XRD pattern of $TiCo_{0.8}Ni_{0.1}Fe_{0.1}Sb$. In the inset the lattice parameters for $TiCo_x(Ni_{0.5}Fe_{0.5})_{1-x}Sb$ are displayed. The line is a result of a linear curve fit.

for the impurity is the forming of the more stable phases due to excess Sb.

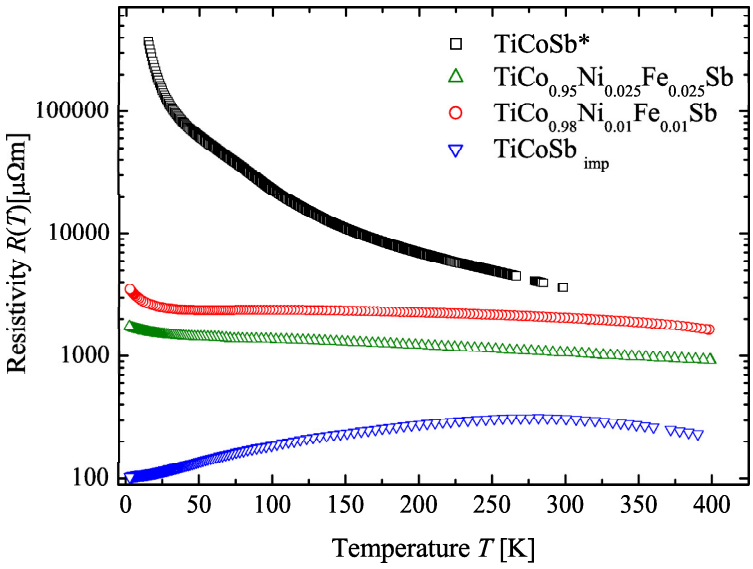

Figure 3.2: Electrical resistivity data for TiCoSb based compounds

3.2.2 Transport Properties

Electrical resistivity

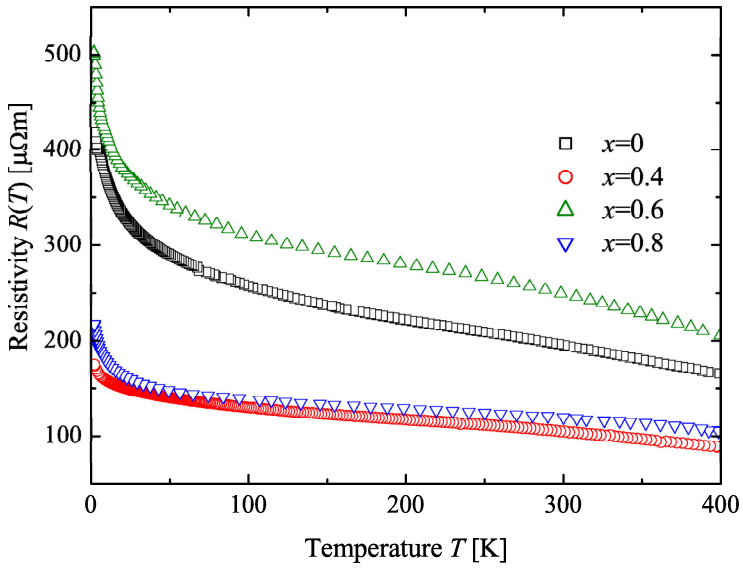

Figure 3.3: Electrical resistivity for $TiCo_x(Ni_{0.5}Fe_{0.5})_{1-x}Sb$

The resistivity was measured in the range from 2 K to 400 K. The determined resistivity values of the first and the last element of the solid solution x=0 and x=1 $TiNi_{0.5}Fe_{0.5}Sb$ [40] and TiCoSb [44, 45] agree well with the findings reported in literature. For TiCoSb a metal to semiconductor transition is observed at about 300 K, which is typical for the as cast arc melt samples. During synthesis Sb is evaporating due to its high vapor pressure. As described in section 2 the losses were compensated but still no full stoichiometry was achieved. For $TiNi_{0.5}Fe_{0.5}Sb$ a typical semiconducting behaviour is observed. In this case the evaporation of Sb during synthesis is negligible compared to the one of the TiCoSb compound. It is assumed that Sb is reacting with either Ni or Fe to a less volatile precursor which prevents the Sb from evaporating. Ni as well as Fe are known to crystallize in orthorombic structures for the composition $NiSb_2$ [46, 47] and $FeSb_2$ [48, 49, 50]. According to reference [15] both TiCoSb and $TiNi_{0.5}Fe_{0.5}Sb$ should be semiconducting because they possess 18 valence electrons. The calculated band gaps are 0.95 eV [33] and 0.8 eV [40] for TiCoSb and $TiNi_{0.5}Fe_{0.5}Sb$, respectively. Therefore, it is assumed that the bandgap decreases with lower Co concentrations. This explains the decrease of the resistivity for a decreasing x in $TiCo_x(Ni_{0.5}Fe_{0.5})_{1-x}Sb$. The opposite is true for the compounds with the Co concentration of 0.95 and 0.98. Here, the resistivity is increased due to the stabilizing

effect of Ni and Fe. This reduces the amount of impurities, that are introduced by the nonstoichiometric amount of Sb. This effect outweighs the reduction of the energy gap.

Thermal conductivity

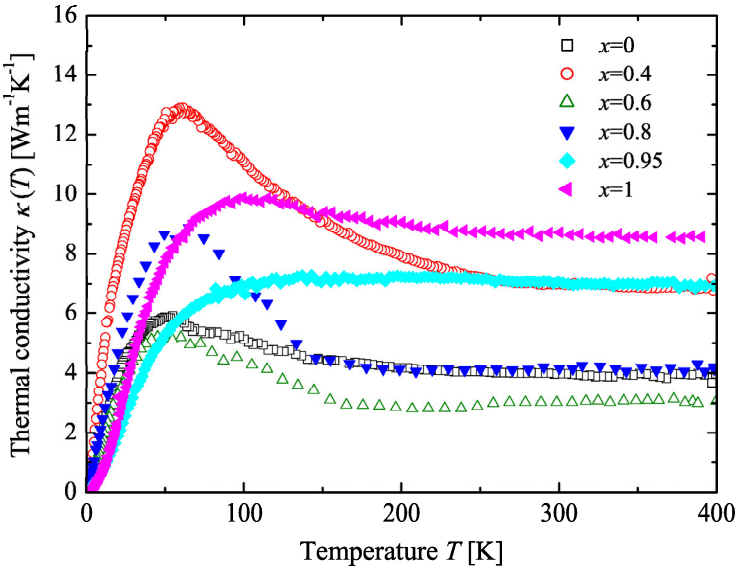

Figure 3.4: Thermal conductivity for $TiCo_x(Ni_{0.5}Fe_{0.5})_{1-x}Sb$

In Figure 3.4 the thermal conductivity measurements of the compounds are displayed. The thermal conductivity was measured in the temperature range from 2 K to 400 K. For the high Co concentrations the thermal conductivity remains nearly unchanged and is decreased a little for x=0.95. No pronounced peak at lower temperatures is observed. For the Co concentrations x=0.8, x=0.6, and x=0.4 the lowest overall thermal conductivities were determined. Additionally a peak at low temperatures is observed, which indicates an only small degree of disorder of the samples. The lowest observed values are about 3 Wm ^{1}K ^{1}, which is among the lowest known values for $C1_b$ compounds. Additionally to a stabilization of the compounds a decrease in the thermal conductivity has been achieved. This decrease can not be explained by only mass fluctuation scattering since the mass differences of Fe, Co, and Ni are small. The introduction of impurities seems unlikely either since a pronounced low temperature peak is observed in the measurement. The reduction of the thermal conductivity for TiCoSb to $TiCo_{0.6}Ni_{0.2}Fe_{0.2}Sb$ equals to a reduction of about 60%. A reduction of the thermal conductivity by the substitution of Fe for Co was reported before by Wu et al [31]. It can be estimated by the Wiedemann-Franz law, that the thermal conductivity is dominated by the lattice thermal conductivity [51]. The reduction is supposed to consist of

several effects which are magnetic scattering of phonons by Fe ions, a small amount of additional impurities, and mass fluctuation.

Seebeck coefficient

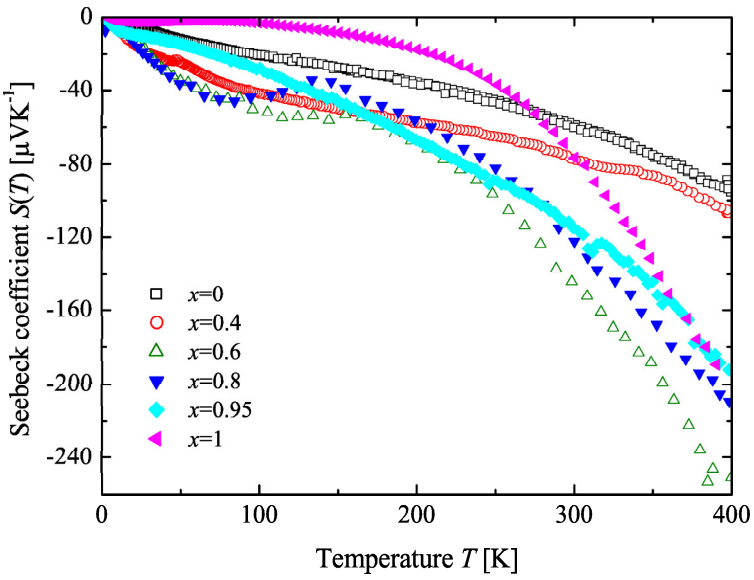

Figure 3.5: Seebeck coefficient for $TiCo_x(Ni_{0.5}Fe_{0.5})_{1-x}Sb$.

In Figure 3.5 the measurements of the Seebeck coefficient in the temperature range from 2 K to 400 K are shown. The values for TiCoSb agree well with the findings of Zhou et al [32]. For $TiNi_{0.5}Fe_{0.5}Sb$ a value of -60μVK^{-1} at 300 K was obtained. This is in disagreement to the value of +30μVK^{-1} reported by Tobola [40]. The Seebeck coefficient for $TiNi_{0.5}Fe_{0.5}Sb$ is very sensitive to the amount of Fe and Ni [40]. This explains the different findings for the Seebeck coefficient. For the Co concentrations of x=0 and x=0.4 the Seebeck coefficient is not significantly influenced. For $TiCo_{0.8}Ni_{0.1}Fe_{0.1}Sb$ and $TiCo_{0.6}Ni_{0.2}Fe_{0.2}Sb$ an increase of the Seebeck coefficient is observed. The raised absolute values of S for $TiCo_{0.6}Ni_{0.2}Fe_{0.2}Sb$, $TiCo_{0.8}Ni_{0.1}Fe_{0.1}Sb$, $TiCo_{0.4}Ni_{0.3}Fe_{0.3}Sb$ at low temperatures are related to a phonon drag [52]. An additional indication for this effect is the pronounced peak of the thermal conductivity in this temperature range for the compounds. The highest achieved Seebeck coefficient increase of about 35% at 400 K was found for $TiCo_{0.6}Ni_{0.2}Fe_{0.2}Sb$ compared to TiCoSb. The negative sign of the Seebeck coefficient indicates that the electric conductivity is dominated by electrons.

The figure of merit of the compounds was calculated in the temperature range from 2 K to 400 K. The results are displayed in Figure 3.6. The biggest improvement compared to TiCoSb was achieved with the compounds $TiCo_{0.6}Ni_{0.2}Fe_{0.2}Sb$ and

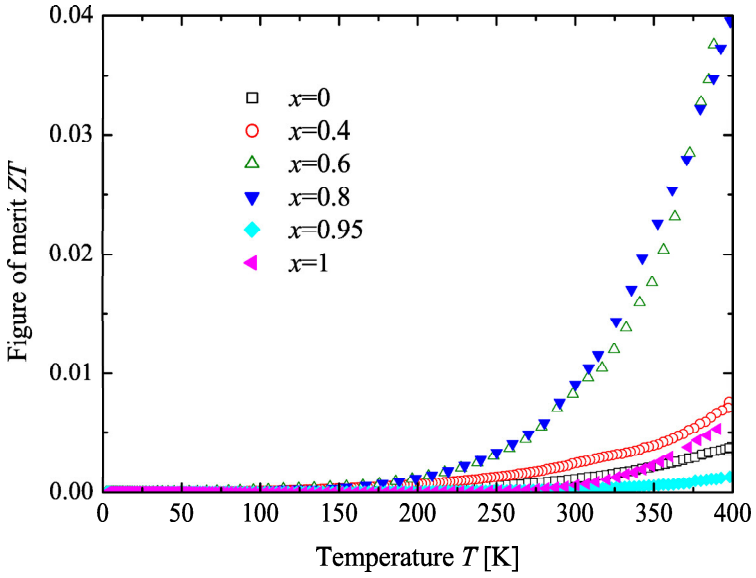

Figure 3.6: Figure of merit for $TiCo_x(Ni_{0.5},Fe_{0.5})_{1-x}Sb$.

$TiCo_{0.8}Ni_{0.1}Fe_{0.1}Sb$. The improvement is mainly based on the reduction of the thermal conductivity and the electrical resistivity.

3.3 Summary and Conclusion

The solid solution $TiCo_x(Ni_{0.5}Fe_{0.5})_{1-x}Sb$ was investigated with respect to its thermoelectric properties. It was shown that the substitution of Co by $(Ni_{0.5}Fe_{0.5})$ effectively enhances the figure of merit. This enhancement is based on the reduction of the thermal conductivity and an increase of the Seebeck coefficient. Furthermore, it was shown that a substitution of Co by equal amounts of Ni and Fe reduces the evaporation of Sb during synthesis and allows a better control of the chemical composition. The highest values for the figure of merit were achieved with the compositions $TiCo_{0.6}Ni_{0.2}Fe_{0.2}Sb$ and $TiCo_{0.8}Ni_{0.1}Fe_{0.1}Sb$. This yielded a value for ZT of approximately 0.04 at 400 K. Although the ZT values have been increased by about a factor of 7 the values are still a magnitude lower than the ones of state of the art materials. Further enhancements can be achieved by the partial substitution of the other constituents in the compound. This is demonstrated in chapter 6.

4 Thermoelectrical and structural properties of $TiCo_{1-x}Ni_xSn_xSb_{1-x}$

4.1 Introduction

Among the most investigated $C1_b$ compounds are TiNiSn [16, 53, 54, 55, 56, 57] and TiCoSb [31, 32, 45, 58]. Both compounds have 18 valence electrons(VE) and are supposed to be small gap semiconductors or semimetals [15]. Both are known to be good thermoelectric materials and have a similar structure and consist of similar elements. In both compounds the 4c Wyckoff position is occupied by Ti atoms. The 4a and 4b Wyckoff positions are occupied by neighbouring atoms of the periodic table. The 4a position is occupied by Co and Ni and the 4b position by Sb and Sn, in TiCoSb and TiNiSn, respectively. The contribution of valence electrons of the elements is displayed in Table 4.1. The substitution of one position in a $C1_b$ compound by the two neighbouring atoms has been successfully applied in the series $Ti(Ni_{0.5}Fe_{0.5})_xCo_{1-x}Sb$ (see chapter 3). The semiconducting properties of the compounds were retained. Based on these results a simultaneous substitution of the 4a and 4b position with a conservation of the 18 valence electrons is conducted. In the series of $TiCo_{1-x}Ni_xSn_xSb_{1-x}$ Ni was partially substituted by Co and to an equal amount Sn by Sb. The number of valence electrons does not change by this substitution, and therefore the semiconducting behavior should be retained. Due to the substitution of 2 positions in the compounds and the accompanying increase of phonon scattering a decrease of thermal conductivity is expected. It is known further that the substitution of Sb for Sn in TiNiSn [59] reduces the thermal conductivity.

4.2 Structural Properties

The series $TiCo_{1-x}Ni_xSn_xSb_{1-x}$ has been prepared by arc melting. X-ray powder diffraction was performed on all compounds. As an example the XRD pattern for $TiCo_{0.2}Ni_{0.8}Sn_{0.8}Sb_{0.2}$ is shown in Figure 4.1. The arrows mark the reflexions arising from the impurity phases. No impurities were detected for the phases with $0 \geq x \geq 0.6$.

Table 4.1: Contribution of the elements to the valence electron count

Compound	X	Y	Z
TiCoSb	4	9	5
TiNiSn	4	10	4

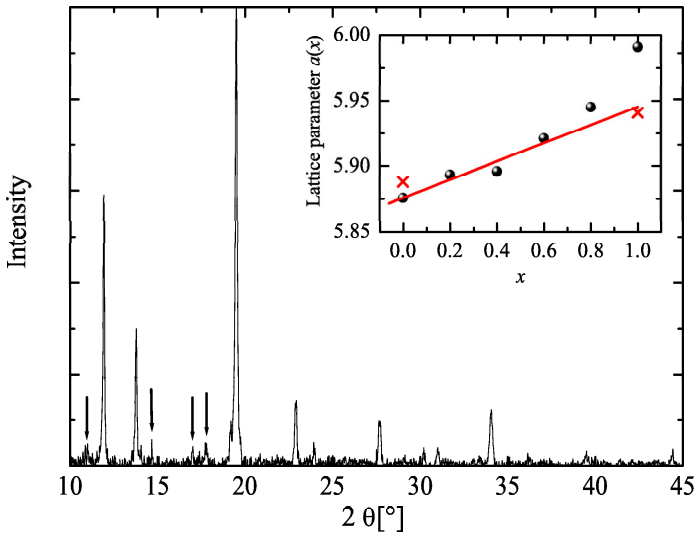

Figure 4.1: XRD pattern for $TiCo_{0.2}Ni_{0.8}Sn_{0.8}Sb_{0.2}$. The arrows denote impurities. The inset shows the lattice parameter a versus the concentration x of $TiCo_{1-x}Ni_xSn_xSb_{1-x}$. The red crosses represent the literature values of the lattice parameter for TiCoSb and TiNiSn.

The amount of impurity is rising with increasing Ni and Sn content for $x > 0.6$. The inset of Figure 4.1 shows the lattice parameter $a(x)$ as a function of the concentration x. The crosses represent the literature values for TiCoSb [41] and TiNiSn [60]. According to Vegard [43] the lattice parameter should linearly increase from TiCoSb to TiNiSn in a solid solution. A linear fit was applied to the data points in the concentration range $0 < x \leq 0.6$. For $x > 0.6$ the data deviates to higher values from the fit with decreasing x. This behavior is related to the increasing amount of impurity observed for a decrease of x. All major phases are of the $C1_b$ structure type. The impurities were identified to be possibly either Sn_5Ti_6 [61], Sn_3Ti_6 [62], $TiNi_2Sb$ [63] or Ni_2TiSn [64]. The same impurities were found for unannealed TiNiSn by Katayama et al [65].

For the investigation of the grain size EDX measurements were performed on $TiCo_{0.1}Ni_{0.9}Sn_{0.9}Sb_{0.1}$ the compound with the lowest thermal conductivity. In Table 4.2 the elemental distribution is shown. The emission lines of Sn and Sb could not be resolved and therefore they are displayed together. The obtained composition is in the expected error range of the measurements. For the determination of the composition the whole field of view of 105×95 μm^2 was used. The micrographs were taken in the Ni Kα, Co Kα, Ti Kα, Sn Lα, Sb Lα lines, and for an integral image. The results are displayed in Figure 4.2. In the micrograph taken in Ti Kα line the distribution of Ti throughout the sample is displayed. The distribution is homogeneous, except for some

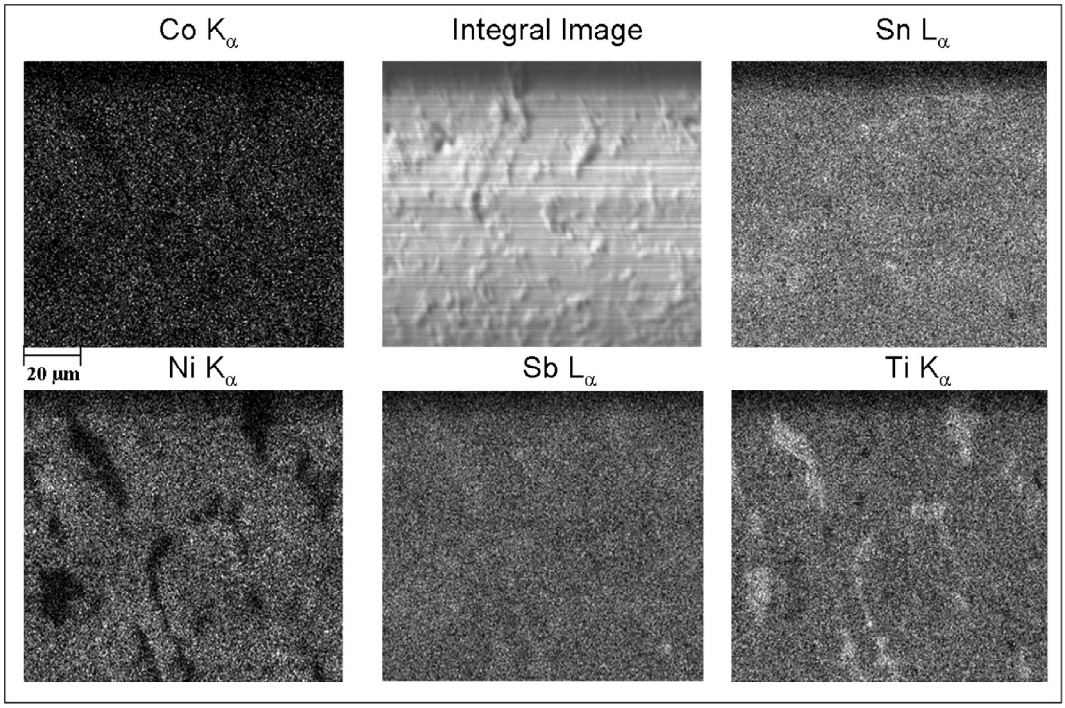

Figure 4.2: EDX measurement of $TiCo_{0.1}Ni_{0.9}Sn_{0.9}Sb_{0.1}$. Displayed are the micrographs taken in the Co K_α, Ni K_α, Ti K_α, Sn L_α, Sb L_α lines and the integral image.

Table 4.2: Atomic percentages of $TiCo_{0.1}Ni_{0.9}Sn_{0.9}Sb_{0.1}$ determined by EDX. Values are given in percent.

	Ti	Co	Ni	Sn+Sb
$TiCo_{0.1}Ni_{0.9}Sb_{0.1}Sn_{0.9}$	100	11	76	76

prolate areas, where an excess for Ti is observed. The prolate areas are oriented from the right lower corner to the left upper corner. At the Ti rich areas deficits of Ni and Co are observed in the respective micrographs. The distributions of Sn and Sb seem to be homogeneous throughout the sample. The prolate structuring is assumed to be caused by the synthesis method. During the melting the upper electrode of the arcmelter is moved in circles above the sample. This leads to a circular convection in the sample, that can result in circular structures. The structures appear prolate, due to the small field of view. These results show that with x values close to 0 the annealing procedure becomes more important. The amount of phase separations increases. This makes a comparison of the thermoelectric properties of unannealed TiCoSb and TiNiSn very difficult.

4.3 Transport Properties

4.3.1 Electrical resistivity

The low to ambient temperature resistivity measurements were performed with the PPMS and in the high temperature measurement range from 340 K to 900 K with the Ozawa RZ2001i unit. The TiCoSb compound shows the metal to semiconductor transition described in Chapter 3. For $0 \leq x \leq 0.4$ the compounds show semiconducting behavior and for $x > 0.4$ the compounds are metallic.

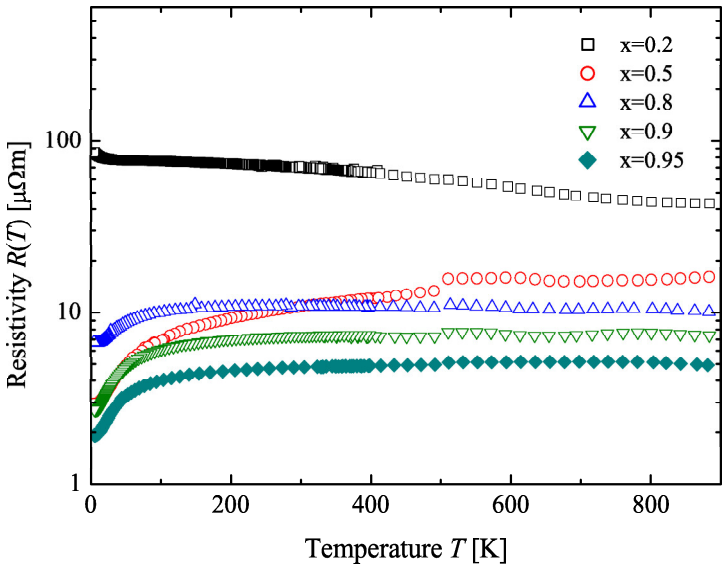

Figure 4.3: Resistivity for $TiCo_{1-x}Ni_xSn_xSb_{1-x}$ in the range from 2 K to 900 K.

The overall resistivity of the compounds is decreasing with increasing x values. It is assumed that for higher Ni and Sn concentrations the disorder in the samples is increased. This leads to a decrease of the gap at the Fermi energy for $0 < x \leq 0.4$. For $x > 0.4$ the gap is closed and the density of states at the Fermi energy is increased. This leads to a reduction of the resistivity and a metallic behavior. Additionally the amount of metallic impurities rises for $x > 0.6$ which leads to an additional reduction of the electrical resistivity. The resistivity measurements show that annealing has a big influence on the electric properties of the samples with high Ni and Sn concentrations [66].

4.3.2 Thermal conductivity

The thermal conductivity for $TiCo_{1-x}Ni_xSn_xSb_{1-x}$ is displayed in Figure 4.4. The highest values for the thermal conductivity are observed for the unsubstituted TiCoSb

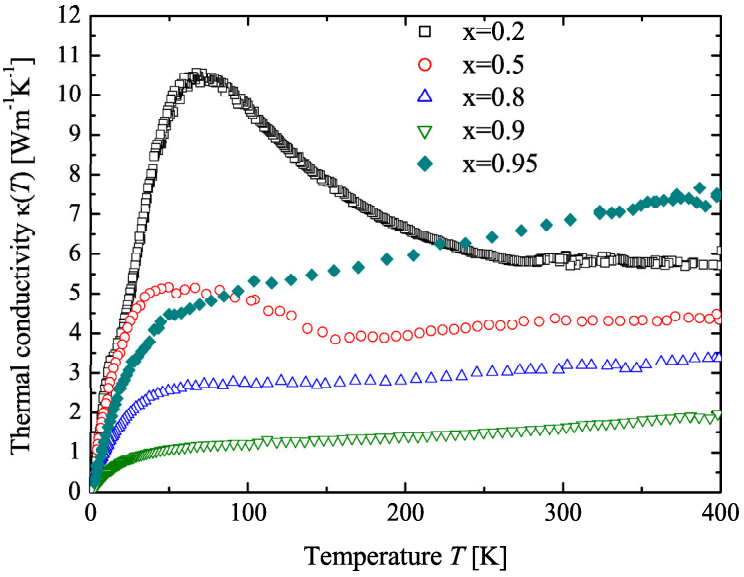

Figure 4.4: Thermal conductivity for $TiCo_{1-x}Ni_xSn_xSb_{1-x}$ in the range from 2 K to 400 K.

compound. With a decrease of the Co and Sb content the thermal conductivity decreases until reaching a minimum for $x \approx 0.9$. For $0 \leq x \leq 0.9$ the thermal conductivity is decreased because the dominating lattice contribution is reduced due to the higher disorder and the inclusion of microstructures in the samples. For $x > 0.9$ the compounds get more metallic and the thermal conductivity becomes dominated by the electronic contribution. The low electrical resistivity leads therefore to high thermal conductivities. It is well known, that substitutions of Sn by Sb reduce the thermal conductivity [16]. The reported reductions were in the range of 0.5 $Wm^{-1}K^{-1}$. Therefore the substitution of Sn by Sb is probably not the sole reason for the reduction of the thermal conductivity. As an additional effect the phonon boundary scattering has to be considered. Its contribution is dependent on the grain size as suggested by Bhattacharya [54]. The prolate Ti rich areas that were observed in the SEM micrographs are supposed to be the origins of the reduction of the thermal conductivity. The phase boundaries act as additional phonon scattering centers and reduce the thermal conductivity.

4.3.3 Seebeck coefficient

The Seebeck coefficient was measured in the low to ambient temperature range with the PPMS and from 340 K to 900 K with the Ozawa RZ2001i unit. The Seebeck coefficient for $TiCo^1$ $^xNi_xSn_xSb_{1-x}$ is displayed in Figure 4.5. The maximum measured value is

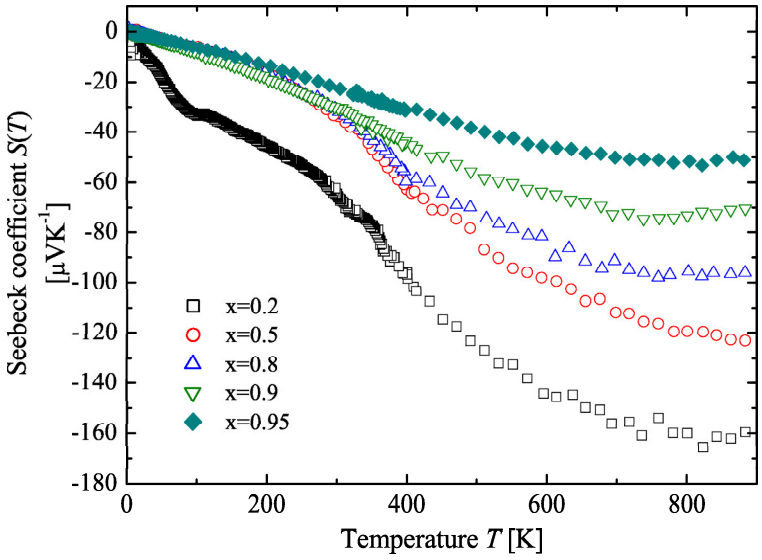

Figure 4.5: Seebeck coefficient for $TiCo_{1-x}Ni_xSn_xSb_{1-x}$ in the range from 2 K to 400 K.

approximately 165 μVK^{-1} at 810 K. The maximum values of the Seebeck coefficients are decreasing with decreasing Co content. The reduction is caused by the increase of the carrier concentration that was observed in the resistivity measurements. The closing of the gap increases the carrier concentration and therefore the absolute values of the Seebeck coefficients are reduced. Further it has to be taken into account that the simultaneous substitution of 2 atoms may have an opposing noncompensating effect on the Seebeck coefficient [67]. The Seebeck coefficient can be also expressed as

$$S = \frac{\sigma_n S_n + \sigma_p S_p}{\sigma_n + \sigma_p}, \tag{4.1}$$

where σ is the electrical conductivity of the electrons and the p or n indices indicate holes and electrons, respectively. If the electrical conductivity of the opposing charge carriers or their Seebeck coefficient become higher the absolute value of the Seebeck coefficient is decreased. This has also to be taken into account for the explanation of the decrease of the maxima of the Seebeck coefficient with decreasing x.

The power factor is calculated by the formula

$$PF = S^2\sigma. \tag{4.2}$$

The results are displayed in Figure 4.6. The power factor yields the highest values for $0.5 \leq x \leq 0.8$ at $\approx$ 900 K. The achieved values are in the range of state of the art materials [68].

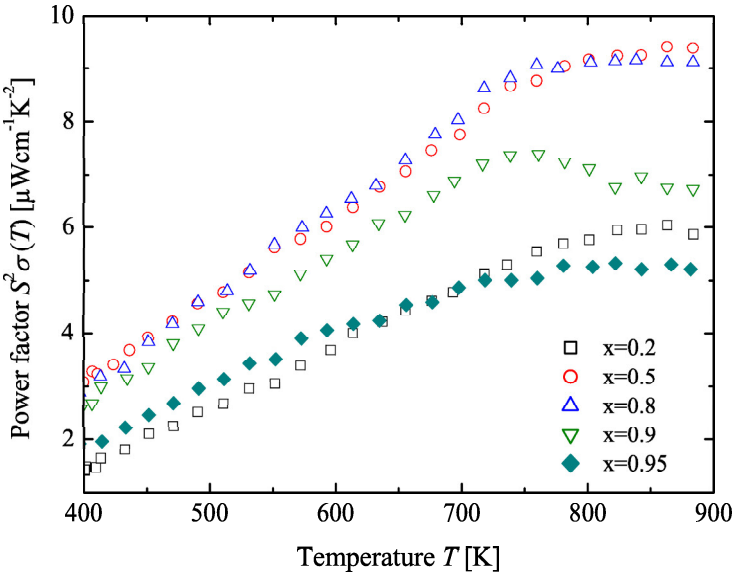

Figure 4.6: The Power factor PF for $TiCo_{1-x}Ni_xSn_xSb_{1-x}$ in the temperature range from 400 K to 900 K.

The observed broad maxima are located between 800 K and 900 K. The great width of the maxima increases the temperature range and therefore the range where thermoelectric generators can be used efficiently. The figure of merit can not be determined directly due to the lack of high temperature thermal conductivity data. Although the thermal conductivity can be estimated. With an assumed constant phononic contribution and a calculated electronic contribution by the Wiedemann-Franz law a thermal conductivity of 4.7 Wm ^{1}K ^{1} at 900 K is calculated for $TiCo_{0.5}Ni_{0.5}Sn_{0.5}Sb_{0.5}$. This results in a figure of merit of $ZT \approx 0.2$ at 900 K.

4.4 Summary and Conclusion

The series $TiCo_{1-x}Ni_xSn_xSb_{1-x}$ was synthesized by arcmelting and its transport properties were determined. The electrical resistivity was measured in the temperature range from 2 K to 900 K. The resistivity behavior changed from semiconducting to metallic with an increase of the Ni and Sn content. The decrease in resistivity is explained by increased disorder and the decrease of the gap at the Fermi energy. The thermal conductivity was investigated in the temperature range from 2 K to 400 K. The lowest value of 2 $Wm^{-1}K^{-1}$ at 400 K was achieved for the composition $TiCo_{0.1}Ni_{0.9}Sn_{0.9}Sb_{0.1}$. This is one of the lowest values reported for a Heusler compound so far. The low value is ascribed to mass fluctuation and point defect scattering as well as phonon scattering at the stripe like Ti rich microstructures. It has been

shown that for Half Heusler compounds a thermal conductivity of 2 Wm ^{1}K ^{1} or less is feasible with an introduction of microstructures. The Seebeck coefficient was investigated in the temperature range from 2 K to 900 K. The highest values were achieved for compositions with a high Co and Sb concentration. Finally, a Power factor of $\approx$ 9.2 μ $Wcm^{-1}K^{-2}$ at 900 K was achieved. This resulted in a calculated figure of merit $ZT = 0.2$ at 900 K, which is in the same order of magnitude as state of the art materials.

5 Thermoelectrical and structural properties of LiXZ

5.1 Introduction

Silicon germanium alloys (SiGe) were first used in space in the SNAP-10A nuclear reactor and have been the exclusive choice for radioisotope thermoelectric generators launched by the U.S. since 1976 [69]. The primary considerations for applications in space are reliability and high operating temperatures. SiGe devices can operate at temperatures up to 1300 K without significant degradation [70, 71, 5]. SiGe thermocouples have accumulated over 250 million device hours in space applications without a single known thermoelectric failure. Although being one of the most used state of the art materials [72, 73, 74] its thermal conductivity is quite high. An effective approach of reducing the thermal conductivity has been applied to the class of Skutterudites [75]. These compounds have voids in their structure that can be filled with guest atoms. The resulting disorder from these inclusions introduces an excellent phonon-scattering mechanism. In this chapter a similar approach is applied to Si and Ge. According to Zintl and Brauer [76] in LiAl Li can transfer its $2s$ electrons to Al which then can form sp^3 bonds as found in Si. If half of the Si atoms in Si are exchanged with LiAl the ternary compound LiAlSi is formed. The resulting compound is of the $C1_b$ structure type. In this chapter Li containing Half Heusler compounds are investigated. The Li atoms are supposed to behave like the described guest atoms of the Skutterudites. Analogously a reduction of the thermal conductivity compared to non Li-containing Half Heusler and Si compounds is expected. In the focus of this chapter are the compounds LiAlSi, LiAlGe and LiGaSi. The series will be further referred to as LiXZ. The similarities between the investigated compounds and Juza-Nowotny compounds [77, 78] are striking. Although the basis for the investigated $A^IB^{III}C^{IV}$ compounds are IV-IV semiconductors whereas the basis for the $A^IB^{II}C^V$ Juza-Nowotny compounds are the III-V semiconductors.

5.2 Results and Discussion

5.2.1 Bandstructure calculations

To provide a basis for the discussion of the electronic properties band-structure calculations were performed. The calculations were performed with the the 'STUTTGART TB-LMTO' program [79]. This code employs the tight-binding linear-muffin-tin orbital

(TB-LMTO) approximation. The calculations were done for the XLiZ series and for LiGaGe, LiInGe, LiInSn, further referred to as the Li$X'Z'$ series. All compounds are cubic and have the space group number 216 (F$\overline{4}$3m) except for the hexagonal LiGaGe which is of the space group number 186 (P63mc). The values for the lattice parameters are taken from the literature references [80, 81, 82, 83, 84, 85]. The number of k-points was set to 12×12×12 and the criterion for charge convergence was set to $10^{-3}e$. The results for the XLiZ series are shown in Figure 5.1.

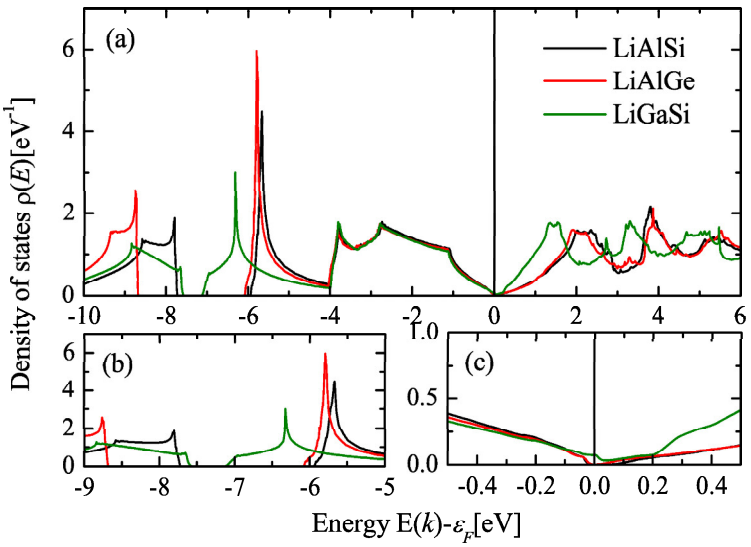

Figure 5.1: Displayed are band structure calculations for Li$X'Z$. In part (a) the whole investigated range is shown, in (b) the low lying band gap at ≈ 7 eV and in (c) the band gap at the Fermi energy.

In part (a) the investigated band structure is displayed from -11 eV to 4 eV. In the parts (b) and (c) the low lying gap at ≈-7.5 eV and the gap at the Fermi energy are highlighted, respectively. The low lying band gap indicates the bond strength between Li and Z. The smaller the band gap the weaker is the bond strength between Li and Z. This means Z can be easily exchanged by Y and therefore disorder in the compound is more likely. The sizes of the low lying band gaps at -8.5 eV and at the Fermi energy are summarized in Table 5.1. If no band gap was found the density of states(DOS) around the Fermi energy is given. For the LiXZ series low lying band gaps are quite large and therefore little disorder is expected. This explains the good agreement of the XRD data with the literature. The case is different for LiGaSi, which has only a small gap and therefore disorder is likely, which can result in a change of the lattice parameter. In part (c) of Figure 5.1 the density of states at the Fermi energy from -1 eV to 1 eV is highlighted. The band gaps are listed in Table 5.1. The values are small

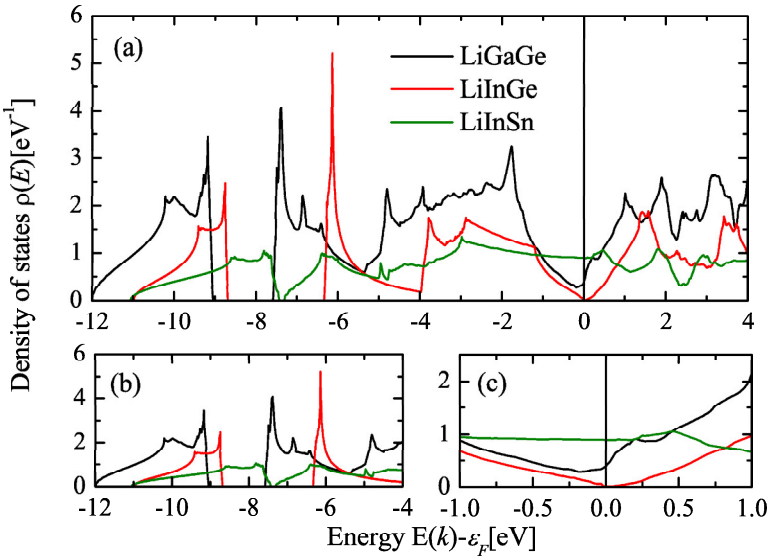

Figure 5.2: Displayed are band structure calculations for LiGaGe, LiInGe, and LiInSn. In part (a) the whole investigated range is shown, in (b) the low lying band gap at $\approx$ 7 eV and in (c) the band gap at the Fermi energy.

Table 5.1: Calculated band gaps for LiXZ and Li$X'Z'$.

Compound	band gap at $\approx$-7.5eV [eV]	band gap at E_F [eV]	DOS at $\approx E_F$
LiAlSi	1.761	0.036	0
LiAlGe	2.592	0.018	0
LiGaSi	0.426	0	0.05
LiGaGe	1.916	0	0.38
LiInGe	2.353	0	0.01
LiInSn	0.083	0	0.89

and indicate, that the materials are semimetals or semiconducters. The value found for LiAlSi agrees approximately with the literature value of 0.1 eV [86]. In Figure 5.2 the results of the band structure calculations for Li$X'Z'$ are displayed. The findings are displayed analogously to the results for LiXZ and are summarized in the second half of Table 5.1. For the low lying band gaps of LiGaGe and LiInGe big values are found, that indicate that the compounds are insusceptible to disorder. For all three compounds no band gap at E_F is found, but the density of states is close to 0 for LiInGe and LiInSn. To verify that the compounds are semiconducting or semimetallic improved band structure calculations have to be performed. The decrease of the gap size at the Fermi energy for the investigated compounds is analogously observed for the Juza-Nowotny compounds. Although the decrease of the band gap size is stronger than the one observed for the Juza-Nowotny compounds.

5.2.2 Structural Properties

X-ray diffraction

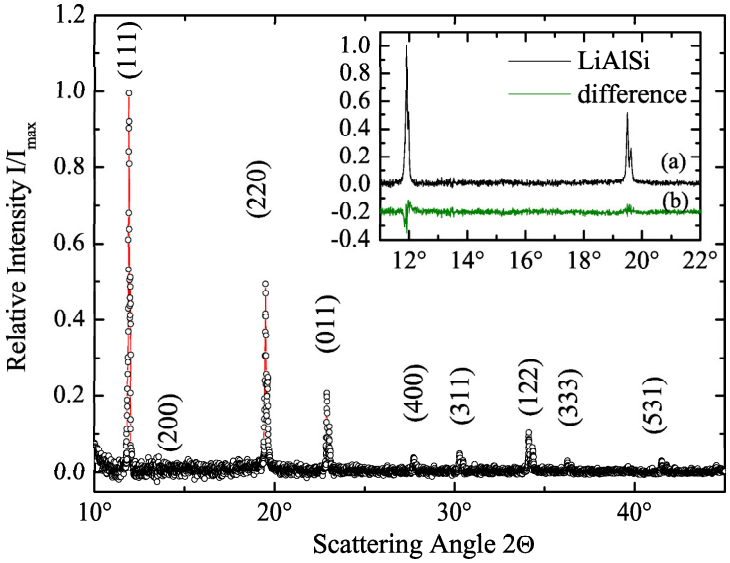

Figure 5.3: XRD pattern for LiAlSi. The inset shows (a) the diffraction pattern and (b) the difference to the Rietveld refinement.

X-ray diffraction was performed on the compounds. For both LiAlSi and LiAlGe the $C1_b$ structure type was identified. The values of the lattice parameters are displayed in Table 5.2. Both values are in very good agreement with data published by other groups [80, 81, 82]. For LiAlSi a Rietveld refinement assuming the $C1_b$ structure type has been performed. The results are displayed in Figure 5.3. The intensities were normalized to the (111) peak and the Wyckoff positions were assumed to be 4a for Li 4b for Al and 4c for Si. Several types of disorder were assumed to improve the agreement of the calculated pattern with the experimentally obtained one. An exchange of Li and Si leads to an enhancement of the (220) peak, therefore this type of disorder can be excluded. An intermixing of Li and Al leads to higher R values with increasing intermixing of the positions. An intermixing seems improbable. An exchange of Al and Si leads to nearly no change in the R value. An intermixing of the positions can therefore not be monitored by XRD. In the inset of Figure 5.3 the XRD pattern (a) and the difference (b) to the Rietveld refinement are shown. For LiGaSi large amounts of impurities of Si and further unidentified phases were found in the XRD patterns. This explains the deviation from the values for the lattice parameters found in literature.

Table 5.2: Lattice parameters for LiXZ. Given are the experimentally determined lattice parameters a_{exp} and the literature lattice parameters a_{lit} for the LiXZ series.

Compound	a_{exp} [Å]	a_{lit}[Å]
LiAlSi	5.922	5.928[80, 81]
LiAlGe	5.977	5.977[82]
LiGaSi	5.429	6.091[82]

Thermal analysis

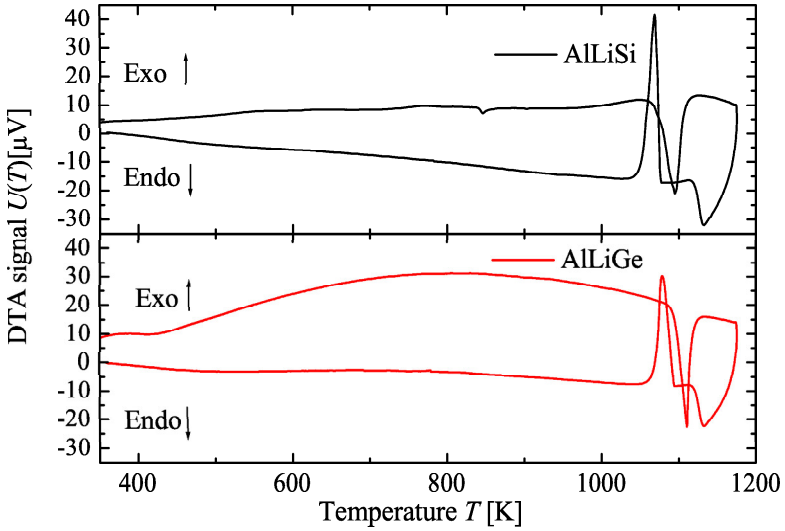

Figure 5.4: DTA measurement for LiAlSi and LiAlGe

The temperature stability was determined by thermal gravimetry(TG) and differential thermal analysis(DTA) in the temperature range from 300 K to 1673 K. A mass loss was observed in the TG measurements for temperatures above 1273 K. Therefore, consequent DTA measurements were limited from room temperature to 1200 K. No mass loss was observed for LiAlSi and LiAlGe in the TG measurements in the reduced temperature range. The results of the DTA measurements for LiAlSi and LiAlGe are displayed in Figure 5.4. The peaks at 1069 K and 1079 K in the cooling curve and the peaks at 1095 K and 1111 K in the heating curve represent the solidification and the melting points of LiAlSi and LiAlGe, respectively. The melting points(T_m) were determined to be 1082 K±4 K for LiAlSi and 1095 K±4 K for LiAlGe. The small peak at about 846 K, that is observed in the measurement of LiAlSi is caused by an impurity. The peak appeared in the heating curve, but was not observed on cooling. It is assumed

that the impurity consisted of unmelted precursor compounds. During the melting of the sample the reaction was completed and LiAlSi was formed. The melting of elements can be excluded as a cause, because none of the used elements melt at the given temperature. Repeated DTA measurements of the same sample yielded reductions of the peak areas by 10%. This is caused by a change of the sample composition. A mass loss was not observed during the measurements. The change of the sample composition is due to a loss of Li. Due to the small mass of Li the loss is not monitored by the TG measurement. The Li either reacts with the sample holder or evaporates and deposits inside the crucible walls. XRD of the heated samples yield increasing amounts of elemental Al and Si for increasing times of heating. This corroborates the assumption that Li loss causes the change of the sample composition and that the compound is not thermally stable in the temperature range. The investigation of LiGaSi was neglected due to its poor thermoelectric properties.

5.2.3 Transport Properties

Electrical resistivity

The electrical resistivity of the compounds was determined in the range from 2 K to 650 K. All compounds exhibit metallic like behavior in the low temperature range. For LiGaSi a transition was observed between 2 K and 6 K in the order of two magnitudes. Superconductivity, like it is reported

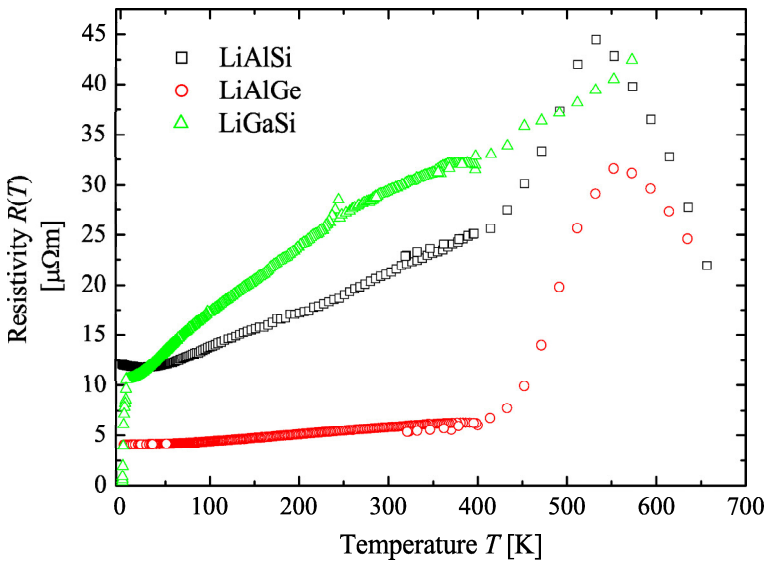

Figure 5.5: Resistivity measurements of LiAlSi, LiAlGe and LiGaSi. Measurements were performed in the range from 2 K to 650 K.

by Kuroiwa [66] for the structurally related NaAlSi was not observed. For LiAlSi and LiAlGe metal to semiconductor like transitions at 530 K and 560 K, respectively, were observed. It was shown by Miura et al [87] that disorder in Heusler compounds leads to a shrinking or even closing of the gap at E_F. Due to the small band gap in LiAlSi even small amounts of disorder yield metallic behavior. Measurements of LiAlSi above 700 K lead to a permanent change of the resistivity and the Seebeck coefficient. The permanent change is ascribed to the high mobility of the Li ions.

Seebeck coefficient

The Seebeck coefficient of the compounds was determined in the range from 2 K to 400 K by the PPMS and from 350 K to 650 K by the RZ2001 unit of Ozawa. All compounds show p-type behavior which indicates a hole dominated conductivity. LiAlSi shows the highest values of 140 μVK^{-1} at 400 K. The values of the other compounds are much smaller with 90 μVK^{-1} at 600 K for LiAlGe and about 30 μVK^{-1} at 550 K at LiGaSi.

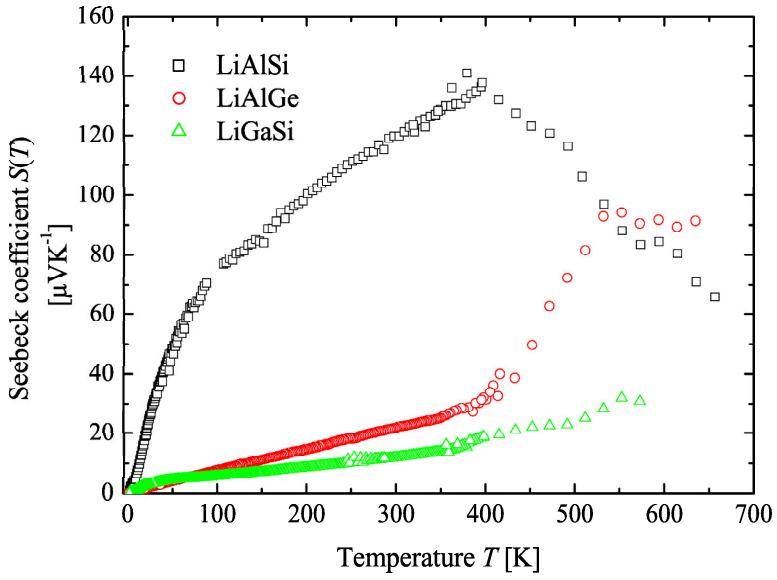

Figure 5.6: Seebeck coefficient measurements of LiAlSi, LiAlGe and LiGaSi. Measurements were performed in the range from 2 K to 650 K.

Thermal conductivity

In the final step the thermal conductivity of the compounds was determined from 2 K to 400 K. For LiAlSi a value of 10 Wm ^{1}K ^{1} at 400 K is found, which is typical for Heusler compounds [32, 88]. LiAlGe has a very low value of 2.4 $Wm^{-1}K^{-1}$ at 400 K.

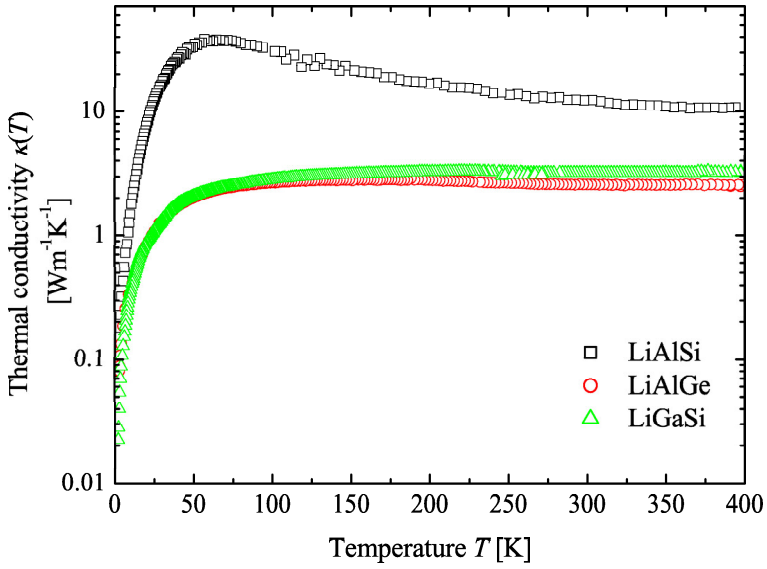

Figure 5.7: Thermal conductivity measurements of LiAlSi, LiAlGe and LiGaSi. Measurements were performed in the range from 2 K to 400 K.

The reduction of the thermal conductivity compared to Si is ascribed to the rattling of the Li atoms. This effect is known from the Skutterudite structure type and has been described by Nolas [75]. The reduction of the thermal conductivity of LiAlGe compared to LiAlSi is probably not based on the different cage size for LiAlGe and LiAlSi. The lattice parameter of LiAlGe is only slightly larger than the one found for LiAlSi. Probably additional mass fluctuation scattering for Ge reduces the conductivity additionally. A similar approach was applied to $Li_xIn_{1-x}Zn_xSb$ [89] which can be viewed as a filled Wurtzite structure. This can be compared to the Half Heusler structure that can be viewed as a Li-filled zinc-blende structure [14, 90]. In the $Li_xIn_{1-x}Zn_xSb$ series In was substituted by Zn and Li. The resulting thermal conductivities are about the same value of 3 $Wm^{-1}K^{-1}$ that were observed for LiAlGe and LiGaSi. The thermal conductivity can be expressed by the sum of a phonon conduction component and an electronic component as

$$\kappa = \kappa_L + \kappa_e. \tag{5.1}$$

κ_e can be described by the Wiedemann-Franz law as $\kappa_e = L\sigma T$, where L is the Lorentz number and σ is the electrical conductivity. κ_e for LiAlSi, LiAlGe, and LiGaSi is 0.29 Wm ^{1}K ^{1}, 1.47 Wm ^{1}K ^{1} and 0.25 Wm ^{1}K ^{1}, respectively. According to Bhandari [3] the highest figures of merit can be achieved with a ratio of 0.5 for κ_e/κ_L. The ratios achieved with LiAlSi, LiAlGe, and LiGaSi are 0.024, 1.313, and 0.084, respectively.

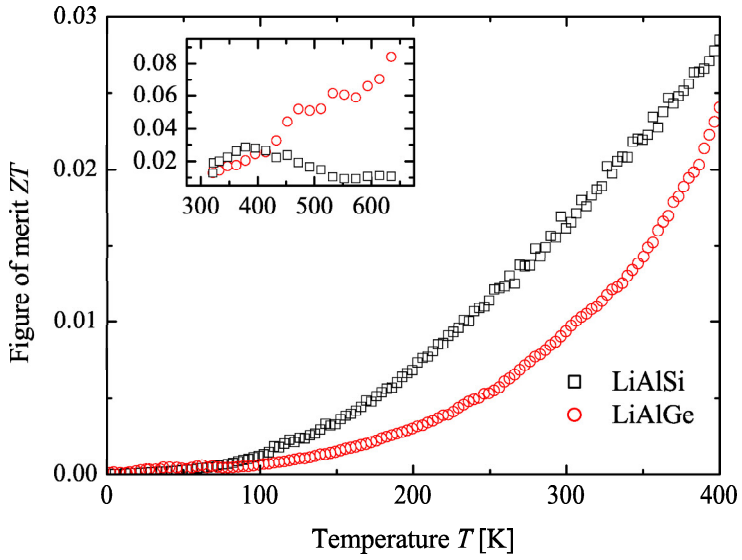

Figure 5.8: Figure of merit for LiAlSi and LiAlGe. The inset displays the high temperature ZT values for an estimated thermal conductivity.

Figure of merit

The figure of merit is displayed in Figure 5.8. It was calculated in the range from 2 K to 400 K from the measurements of the thermoelectric properties. The highest ZT values are reached for LiAlSi at 400 K, where the Seebeck coefficient reaches its maximum. For LiAlGe the Figure of merit is smaller, due to the smaller value of the Seebeck coefficient. The thermal conductivity is strongly reduced, but that can not compensate the decrease of the Power factor. In the inset of Figure 5.8 the ZT values are displayed for the high temperature measurements. Since the thermal conductivity for the high temperature part is not known, an approximation was used. The thermal conductivity was assumed to be constant from 400 K on. The constant was determined by the averaging of the highest 5 measured values. The respective values are 10.7 $\mathrm{Wm^{-1}K^{-1}}$ and 2.55 Wm ^{1}K ^{1} for LiAlSi and LiAlGe, respectively.

5.3 Summary and Conclusion

The Seebeck coefficient and the resistivity of LiAlSi, LiAlGe and LiGaSi were investigated in the temperature range from 2 K to 650 K. The thermal conductivity was measured in the temperature range from 2 K to 400 K. Moderate resistivities in the range from 4 to 45 $\mu\Omega$m were observed. The highest Seebeck coefficient of 160 $\mu\mathrm{VK^{-1}}$ was measured for LiAlSi at 400 K, which makes it the most promising of the Li containing compounds. The rattling approach that has been applied to the Skutterudites [91]

has been transferred successfully to the Half Heusler compounds. It resulted in a strong decrease of the thermal conductivity for all compounds except LiAlSi. The figure of merit is the highest for LiAlSi in the low temperature range from 2 K to 400 K even though the thermal conductivity is quite high. For higher temperatures the figure of merit of LiAlGe is higher. The thermal conductivity can be reduced by a partial replacement of Si with Ge. The electron concentration has to be optimized further. This can be achieved by the partial substitution of Si or Ge with Al or Ga for p-type carriers. For a n-type substitution Al and Ga can be replaced with Si or Ge. The effective reduction of the thermal conductivity for LiAlGe compared to LiAlSi is about 80%. Even higher percentages may be reached when Half Heusler compounds with heavier atoms are investigated, like LiInGe [83] or LiInSn [84]. If this approach can be successfully applied to state of the art Heusler compounds with conservation of their high power factors the figure of merit will be significantly enhanced.

6 TiCoSb based compounds

6.1 Introduction

In this chapter the properties of several TiCoSb based compounds are presented. In the solid solution $Co_{1+x}TiSb$ additional Co was introduced into the compound and its effect on the thermoelectric properties was investigated. The addition of Co introduce additional scattering centres into the compound. This increases the phonon scattering and reduces the thermal conductivity. Further, the addition of Co as an acceptor element influences the electronic properties of the compound significantly. In the solid solution $Co_{1-y}Cu_yTiSb$ the substitution of Co by Cu was investigated. Since Cu adds 2 electrons per atom to the structure a very sensitive behaviour upon substitution is expected. The impact on the thermoelectric properties is shown. In the solid solution of $CoTiSb_{1-z}Bi_z$ Sb was substituted by Bi. The substitution of Sb by the homologous Bi is expected to reduce the thermal conductivity due to the higher mass of Bi. Since the number of valence electrons is not changed by the substitution the change in band structure is supposed to be small. The influence of the substitution of Bi on the thermoelectric properties is presented. For the sake of clarity a list of the synthesized compounds is displayed in Table 6.1.

Table 6.1: Table of synthesized compounds

$TiCo_{1+x}Sb$	$TiCo_{1-y}Cu_ySb$	$TiCoSb_{1-z}Bi_z$
TiCoSb	”	”
$TiCo_{1.05}Sb$	$TiCo_{0.98}Cu_{0.02}Sb$	$TiCoSb_{0.95}Bi_{0.05}$
$TiCo_{1.1}Sb$	$TiCo_{0.97}Cu_{0.03}Sb$	$TiCoSb_{0.9}Bi_{0.1}$
$TiCo_{1.2}Sb$	$TiCo_{0.96}Cu_{0.04}Sb$	$TiCoSb_{0.85}Bi_{0.15}$
$TiCo_{1.4}Sb$	$TiCo_{0.95}Cu_{0.05}Sb$	-
$TiCo_2Sb$	-	-

6.2 Results and Discussion

6.2.1 The series $TiCo_{1+x}Sb$

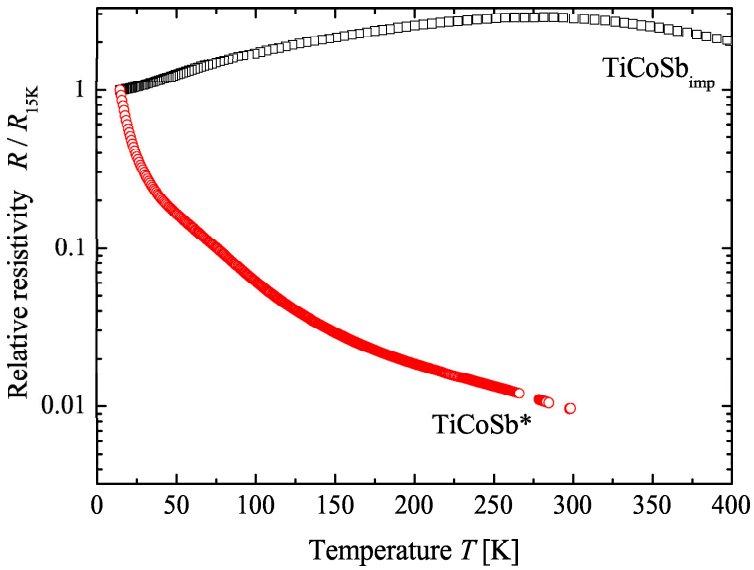

Figure 6.1: Resistivity for TiCoSb* and $TiCoSb_{imp}$

TiCoSb is a 18 valence electron (VE) semiconductor with a band gap of about 0.95eV [33, 34]. If the number of valence electrons deviates from 18 or if impurities are introduced the gap is assumed to be reduced and for larger amounts of disorder it may be even closed. For small impurity amounts the resistivity shows metal to semiconductor transitions and for larger amounts of impurities the resistivity behavior changes to metallic. During synthesis Sb is likely to evaporate, due to its low boiling point. This results in nonstoichiometric compositions and a deviation from the 1:1:1 composition. For comparison the resistivity measurements of a pure semiconducting compound TiCoSb* and a nonstoichiometric compound $TiCoSb_{imp}$ are displayed in Figure 6.1. Resistivity data of TiCoSb* are taken from [92]. In this chapter the structural and thermoelectric properties of $TiCo_{1+x}Sb$ are reported. X-ray diffraction(XRD) was performed to investigate the structure of the compounds. All compounds were determined to be of the $C1_b$ structure type. As an example the XRD pattern for TiCoSb is shown in Figure 6.2. A Rietveld refinement was performed on the XRD pattern and a lattice parameter of 5.882 Å was found. This is in agreement with the values of 5.979 Å [42] and 5.884 Å [41] reported in literature. For the Rietveld refinement the occupation of the positions was assumed to be 4a for Ti, 4b for Sb and 4c for Co. The smallest differences between the refinement and the experimental pattern were found for an assumed antisite disorder

Table 6.2: Theoretical and experimental values for XRD intensity.

	theo. TiCoSb	exp. TiCoSb	theo. $TiCo_{1.6}Sb$	exp. $TiCo_{1.6}Sb$
(111)	0.43	0.5	0.2	0.69
(200)	0.27	0.24	0.09	0.39
(222)	1	1	1	1

of 8% between the 4b and the 4c position. The inset of Figure 6.2 shows the lattice parameter versus the Co concentration x. For x=0, 0.2, 0.4 the solid solution is following Vegard's law [43] and the lattice parameter is decreasing linearly with increasing x. For $x \geq 0.6$ Vegard's law is not satisfied anymore. Therefore, it is assumed that additonal Co can be introduced into TiCoSb only up to 40 %. No other phase is observed in the XRD patterns. For an increasing Co content in $TiCo_{1+x}Sb$ the intensity of the (111) and (200) peaks is supposed to be reduced. This is not observed in the XRD patterns. For TiCoSb the calculated and experimentally determined intensities agree nicely. For $TiCo_{1.6}Sb$ the experimentally determined values behave opposite to the theoretically predicted ones. It is assumed, that the Co, which can not be inserted into the sublattice of TiCoSb is separated and aggregates on the sample surface. This is supported by XPS measurements, that yield a maximum of x=0.4 ± 0.1 for $TiCo_{1+x}Sb$ for measurements of the bulk.

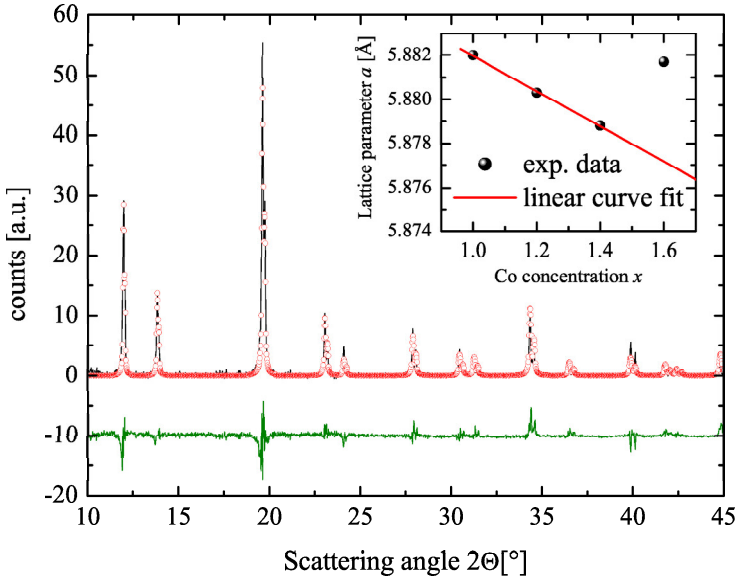

Figure 6.2: XRD of TiCoSb. The black line represents the measured XRD pattern and the red dots the refined pattern. Below that the difference of the two is displayed. The inset shows the lattice parameter versus the concentration x of Co.

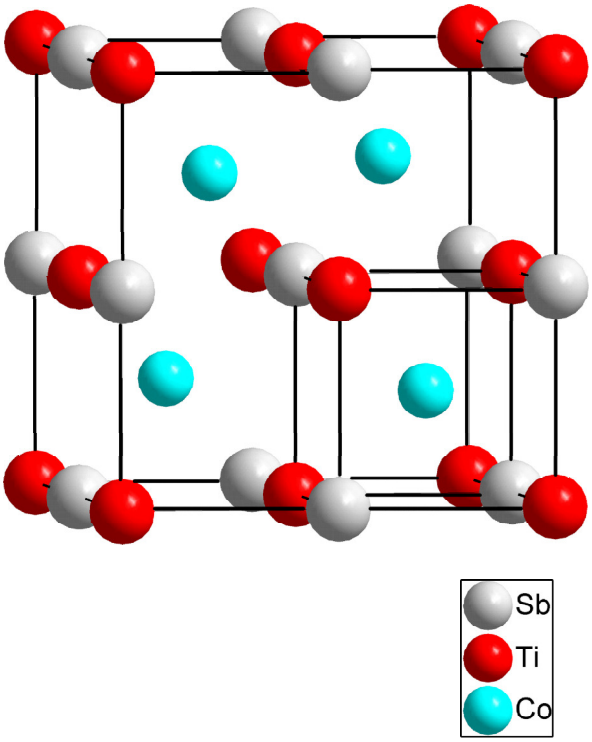

Figure 6.3: Unit cell for TiCoSb

For the explanation of the decreasing lattice parameter in $TiCo_{1+x}Sb$ with increasing x the model created by Boff et al for Heusler [93] compounds was used. TiCoSb consists of an fcc lattice made of Co atoms. Inside this fcc lattice there is a smaller bcc lattice (box) having Ti and Sb atoms at the corners(4a and 4b Wyckoff positions) and alternatingly a Co atom and a vacancy at its centre (8c Wyckoff position) see Figure 6.3 for comparison. Elastic forces in such a situation are supposed to be transmitted from the bcc lattice to the fcc lattice, increasing or decreasing its equilibrium lattice parameter in response. For x=0 in $TiCo_{1+x}Sb$ the 8c position is only half filled with Co. For increasing x the vacant 8c positions are filled with Co. The Co acts as an electron acceptor and attracts electrons from the atoms at the 4b and 4a positions. This leads to an increased Coulomb exchange of the bcc lattice with the 8d positions and a reduction of the lattice parameter. Further, the gap at the Fermi energy is closed with increasing amounts of Co leading to a metallic compound as shown in the resistivity measurements in Figure 6.4. The resulting higher electron mobility ensures the overall charge neutrality in the compound.

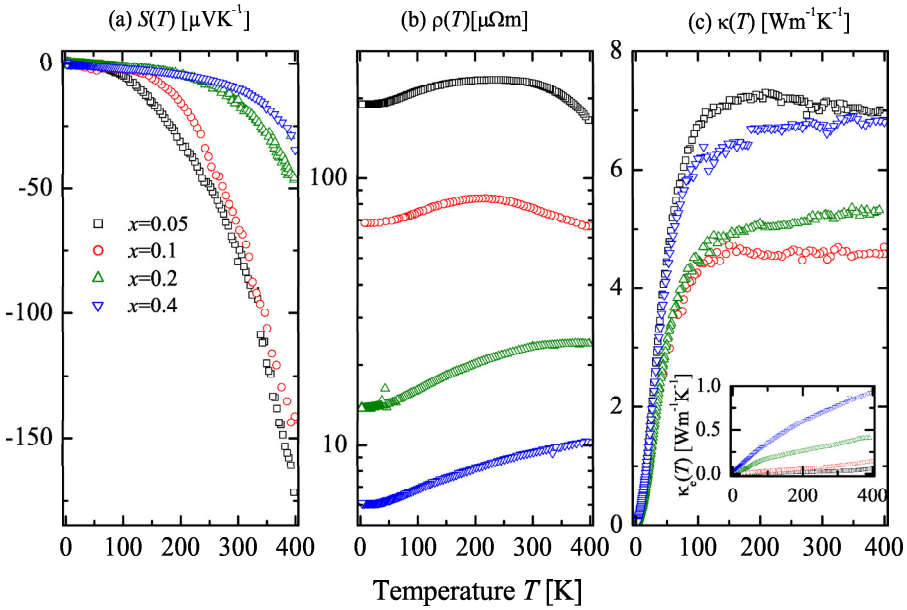

Figure 6.4: Thermoelectric properties of $TiCo_{1+x}Sb$. Given are (a) the Seebeck coefficient $S(T)$, (b) the resistivity $\rho(T)$, and (c) the thermal conductivity $\kappa(T)$. Note the logarithmic scale for the resistivity. The inset shows the electronic part of the thermal conductivity κ_e.

The thermoelectric properties of the solid solution $TiCo_{1+x}Sb$ are displayed in Figure 6.4. In part (a) of the graph, the Seebeck coefficient is displayed. With an increasing amount of Co the Seebeck coefficient declines as it is expected for higher carrier concentrations [26]. In part (b) of the graph the resistivity is displayed. The resistivity decreases with increasing amounts of Co. It is assumed, that the additional Co either creates bands in the gap at the Fermi energy or leads to a smearing of the valence and conduction bands. Band structure calculations for a 5% swapping of the atoms and a 5% surplus of Co have been carried out by Balke et al [34]. The calculations showed that even for an only 5% swapping of the atoms the band gap at the Fermi energy is destroyed. The thermal conductivity is displayed in (c). The minimum value is reached at 10% additional Co content. It is assumed, that the lowering of the thermal conductivity is caused by the partial filling of the fcc sublaticce. The total thermal conductivity can be described as $\kappa = \kappa_e + \kappa_l$, where κ_e is the electronic and κ_l the lattice contribution. By this formula and the Wiedemann Franz law $\kappa_e = L\sigma T$, with L being the Lorentz number, σ the electric conductivity, and T the temperature, κ_e and κ_l were determined. The results are displayed in the inset of Figure 6.4. The electronic contribution to the thermal conductivity is increasing with with increasing x. For temperatures above 200 K the electronic contribution to the thermal conductivity becomes higher. This is reflected in the increasing slopes for $T > 200$ K with increasing x.

6.2.2 The series $TiCo_{1-y}Cu_ySb$

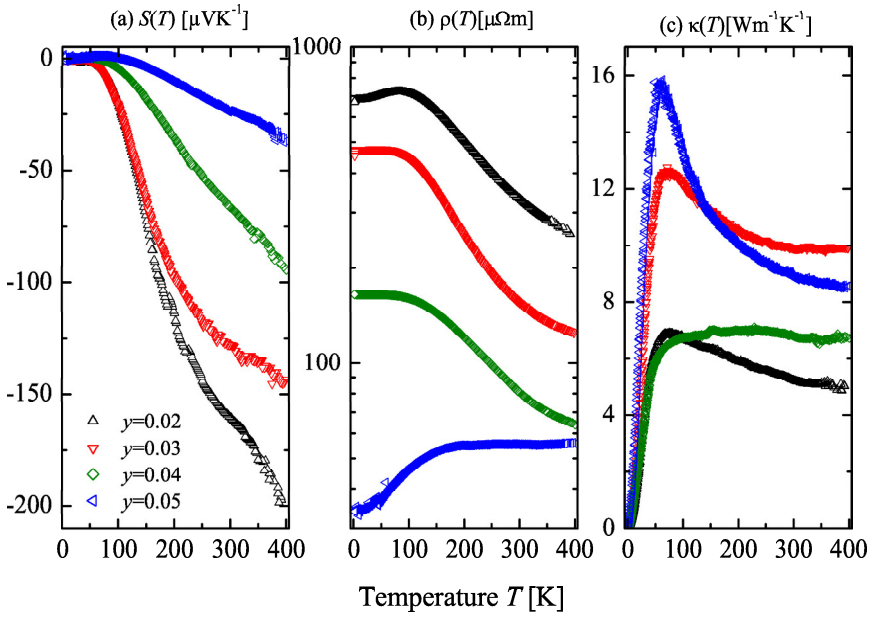

Figure 6.5: Thermoelectric properties of $TiCo_{1-y}Cu_ySb$. Graph a) shows the Seebeck coefficient $S(T)$, b) the resistivity ρ, and c) the thermal conductivity $\kappa(T)$.

The thermoelectric properties of the solid solution $TiCo_{1-y}Cu_ySb$ are displayed in Figure 6.5. Due to the 2 excess valence electrons of Cu compared to Co, and the resulting big impact on the electronic structure, small variations for y were used. Rietveld refinements were performed on the XRD patterns. For all compounds the lattice parameter was constant within the error range with a value of 5.881 Å± 0.002 Å. In 6.5 (a) the Seebeck coefficient is displayed. The highest values of $S(T)$ are reached at 400 K. The Seebeck values are rapidly decreasing with increasing Cu content. In 6.5 (b) the electrical resistivity is displayed. The electrical resistivity is decreasing with higher Cu contents. The substitution of Co by Cu leads to a diminishing of the metal to semiconductor transition. At 5% Cu content the semiconducting behavior has changed to a metallic one. In 6.5 (c) the thermal conductivity is displayed. The values vary from 6-10 $Wm^{-1}K^{-1}$ for the compounds. The thermoelectric properties are highly sensitive to the Cu substitution. The results are in agreement with the findings of Stopa et al [94].

6.2.3 The series $TiCoSb_{1-z}Bi_z$

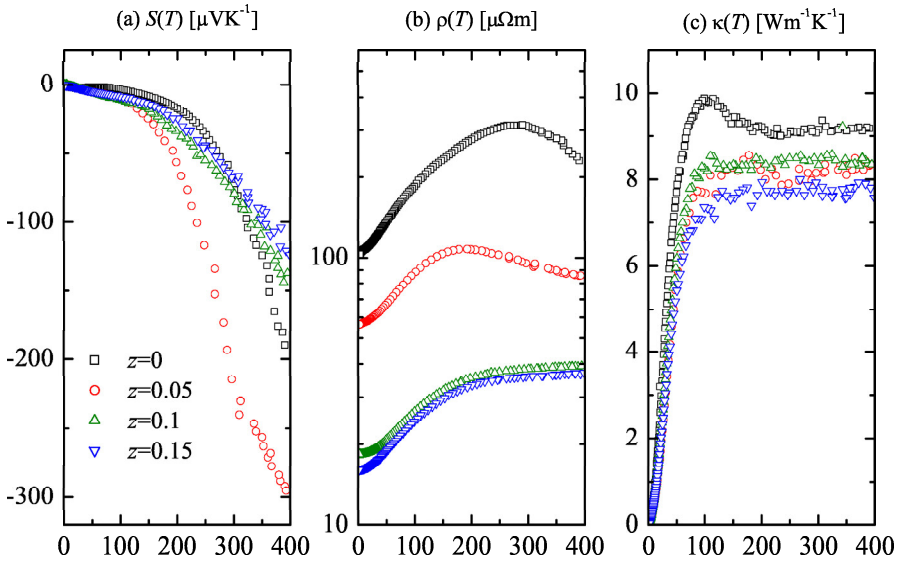

Figure 6.6: Thermoelectric properties of $TiCoSb_{1-z}Bi_z$. Graph (a) shows the Seebeck coefficient $S(T)$, (b) the resistivity $\rho(T)$, and (c) the thermal conductivity $\kappa(T)$.

This chapter reports on the thermoelectric properties of the solid solution $CoTiSb_{1-z}Bi_z$. Both Sb and Bi have a lower boiling point than the melting point of Co. This leads to an evaporation of the elements before the compound is formed. Due to the evaporation and the small amount of Bi in the samples the uncertainty regarding the true composition of the compounds is increased. Therefore the values chosen for z were 5, 10, and 15. The melting and boiling points of the used elements are given in Table 6.3. For structural investigations XRD was performed. XRD yielded lattice parameters a_{exp} of 5.880 Å± 0.001 Å for the compounds. Since the amount of substitution is small the results are in agreement with Vegard's law for solid solutions [43]. No impurities were observed in the XRD patterns. The thermoelectric properties of the solid solution $CoTiSb_{1-z}Bi_z$ are displayed in Figure 6.6. In Figure 6.6 (a) the Seebeck coefficient is shown. The highest value for the Seebeck coefficient is found at 400 K for all compounds. For $CoTiSb_{0.95}Bi_{0.05}$ a value of -300 μVK^{-1} at 400 K is found, while for $x = 0.1$ and 0.15 the value is a lot smaller. In Figure 6.6 (b) the resistivity is displayed. The resistivity is decreasing with increasing Bi percentages z. The metal to semiconductor transition of CoTiSb which is at 290 K shifts to lower temperatures for $CoTiSb_{0.95}Bi_{0.05}$ at about 190 K. For $CoTiSb_{0.9}Bi_{0.1}$ and $CoTiSb_{0.85}Bi_{0.15}$ the resistivity is metallic. In Figure 6.6 (c) the thermal conductivity is displayed. The thermal conductivity decreases slightly

with increasing Bi content. This is expected due to the increased phonon scattering at the heavier Bi atoms compared to the lighter Sb atoms.

Table 6.3: Melting points (m.p.) and boiling points (b.p.) of the used elements [95]

element	m.p. [°C]	b.p. [°C]
Co	1495	2927
Ti	1668	3287
Sb	630.63	1887
Bi	271.4	1564

The substitution of Sb by Bi is isoelectronic and therefore the influence on the electronic properties is expected to be small. For $x \geq 0.1$ the compounds show metallic resistivity and the band gap is closed. The band structure around the Fermi energy does not change either, as the Seebeck coefficient does not change from x=0.1 to x=0.15. For x= 0.05 the situation is different. The metal to semiconductor transition shifts to lower temperatures indicating less disorder and/or less impurities in the sample. At the same time the resistivity is reduced and the Seebeck coefficient is increased. This is unexpected due to the dependency of both properties on the carrier concentration n. For further investigations band structure calculations of TiCoSb and $TiCoSb_{0.85}Bi_{0.15}$ were carried out. The details of the calculations can be taken from the publication by Balke et al [34]. The calculated densities of states for TiCoSb and $TiCoSb_{0.85}Bi_{0.15}$ are displayed in Figure 6.7. For comparison the total density of states and the density of states for Sb and Bi for both compounds are displayed.

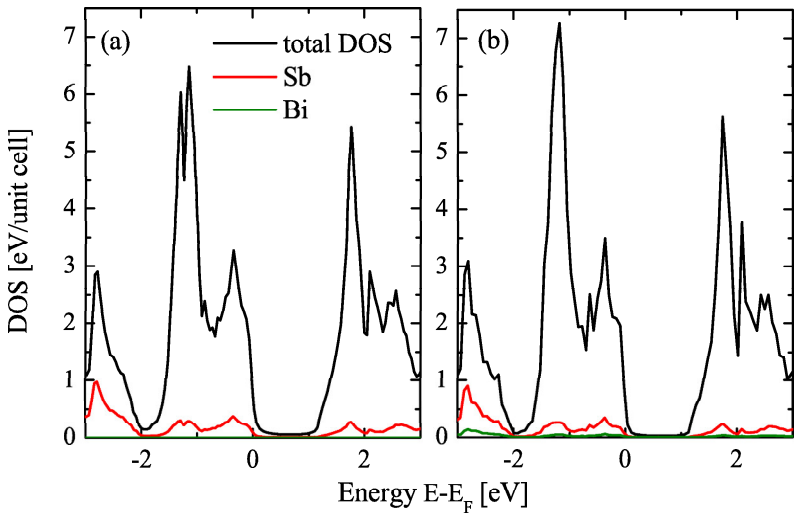

Figure 6.7: Calculated density of states (DOS) for (a) TiCoSb and (b) $TiCoSb_{0.85}Bi_{0.15}$.

The total DOS of both compounds is very similar. A significant difference of the total DOS is only observed for the low lying Bi s and p-bands at -10.9 eV. The size of the band gap at the Fermi energy does not change and the influence of the Bi on the valence and the conduction band is small. The behavior of $TiCoSb_{1-z}Bi_z$ can be explained by assuming a heavily doped semiconductor with compensating n- and p-type carriers. Heavier effective mass n-type carriers dominate the Seebeck coefficient and higher mobile p-type carriers dominate the electrical conductivity. Appropriate to a two-band conduction model, the Seebeck coefficient is written as $S = (S_p\sigma_p + S_n\sigma_n)/(\sigma_p + \sigma_n)$, where S is the Seebeck coefficient, σ is the electrical conductivity ($\sigma = 1/\rho$, ρ is the electrical resistivity) and the indices p and n denote the carrier type, hole or electron, respectively [26]. If S_p and S_n change only little with the substitution of Bi then the relative change of the conductivities n- and p-type to n-type also explains the change of the Seebeck coefficient. Further increases in n-type doping are possible and higher Seebeck coefficients can be reached by a reduction of the compensation effect of the p-type carriers. However this occurs at the cost of high n-type carrier concentrations that reduces S_n as observed for $TiCoSb_{0.9}Bi_{0.1}$ and $TiCoSb_{0.85}Bi_{0.15}$.

6.2.4 Figure of merit

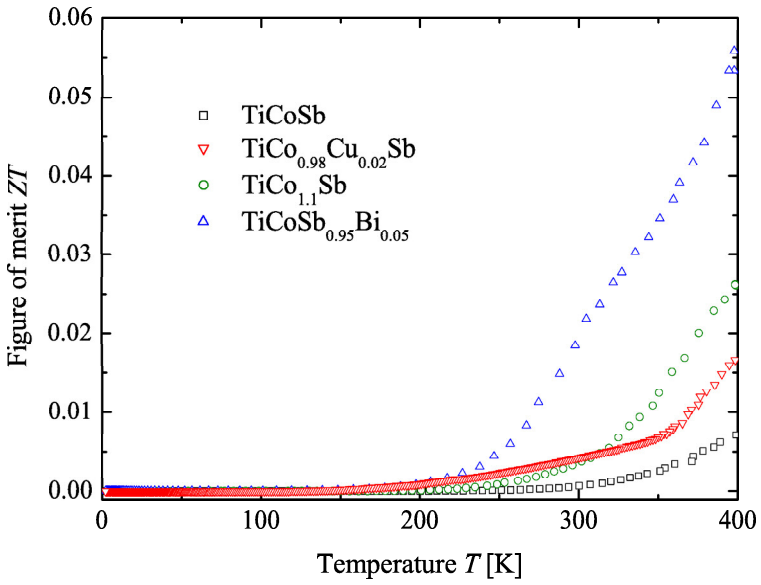

Figure 6.8: Shown is the figure of merit for the highest ZT value of each series.

In this subsection the achieved figures of merit are compared. The values of the highest figure of merit for each series is found in Figure 6.8. For all substitutions the figure of merit is increasing for higher temperatures up to a temperature of 400 K. For all

substitutions an increase of the figure of merit compared to the basic TiCoSb compound was achieved. The highest increase was found for $TiCoSb_{0.95}Bi_{0.05}$, which is based on the enlargement of the Seebeck effect and parallel reduction of the electrical resistivity.

6.3 Summary and Conclusion

In this chapter several solid solutions of compounds based on TiCoSb were synthesized and thermoelectrical investigations were performed. The synthesized solid solutions are $TiCo_{1+x}Sb$, $TiCo_{1-y}Cu_ySb$, and $TiCoSb_{1-z}Bi_z$. XRD was performed to check the structure type and to determine the lattice parameters of the compounds. For all phases the $C1_b$ structure type was determined and a lattice parameter of 5.880 ± 0.001 was found. The thermoelectric properties were measured for all compounds in the temperature range from 2 K to 400 K. The investigation of the $TiCo_{1+x}Sb$ resulted in an optimization of the figure of merit for x=0.1. The optimization is mainly based on the reduction of the electrical resistivity and thermal conductivity while nearly retaining the Seebeck coefficient. For $TiCo_{1-y}Cu_ySb$ the smallest improvement of the ZT value was achieved. The electrical resistivity was reduced, as was the Seebeck coefficient. Each effect nearly compensated the other and therefore the change of the ZT values is small. Cu does not seem to be a suitable replacement for Co to improve the thermoelectric properties. Additional substitutions [32, 58] can be performed to improve ZT or to change the sign of the Seebeck coefficient [96, 97, 98]. The biggest improvement of ZT was achieved in the solid solution $TiCoSb_{1-z}Bi_z$ for z=0.05. The Seebeck coefficient was increased with a simultaneous reduction of the electrical resistivity. The thermal conductivity was nearly unchanged. The thermal conductivity can be further reduced by using nanoparticles of the compounds [52]. Bi seems to be a suitable substitution for Sb to increase the ZT value. Although the synthesis is complicated due to the high evaporation rates of Sb and Bi the results are very promising.

7 Theoretical and experimental characterization of Co_2TiZ

7.1 Introduction

In 1983, the band structures of Mn-based Heusler alloys of the $C1_b$ crystal structure were calculated by de Groot [99]. Some of these compounds show unusual electronic properties. For the majority spin electrons the density of states is bigger than zero and for the minority spin electrons the density of states is equal to zero. This new material class was further referred to as half metallic ferromagnets (HMF). A drawing of the theoretical model is shown in Figure 7.1.

It was recognized by Kübler et al [100] that the Heusler compounds Co_2MnAl and Co_2MnSn are half metallic ferromagnets by the definition of de Groot. It was concluded that this kind of electronic structure should lead to peculiar transport properties because of the opposing behavior of the electrons in the majority and minority channel. The ratio of electrons in the majority channel to the electrons in the minority channel at the Fermi energy is called degree of spin polarization. Compounds with a high degree of spin polarization are proposed as materials for spin injection devices [99]. A further requirement for the use as a material in a spin injection device is a sufficiently high Curie temperature. For this reason Heusler alloys of the $L2_1$ structure type have attracted interest. Some of these compounds exhibit high Curie temperatures and according to theory they have a high spin polarization [101, 102] at the Fermi energy.

In this chapter the properties of the Heusler compounds Co_2TiZ (Z = Si, Ge, Sn) are investigated theoretically and experimentally. The compounds were synthesized by arcmelting and consequent annealing at 1073 K for two weeks. Since the compounds are supposed to be halfmetallic ferromagnets all calculations are carried out for majority and minority electrons. The calculated results are compared to the experimental results and are discussed in the respective subchapters. X-ray diffraction was performed for the structure determination and the obtained cell parameters were set into context to other Heusler compounds with similar compositions. For the surface investigations energy dispersive X-ray spectroscopy (EDX) was used to ensure the homogeneity of the samples. The magnetic properties as well as the obligatory transport measurements were performed. In a final characterization step Hard X-ray Photo Emission Spectroscopy(HAXPES) was performed on the compounds to experimentally determine the band structure and compare it to the calculated results.

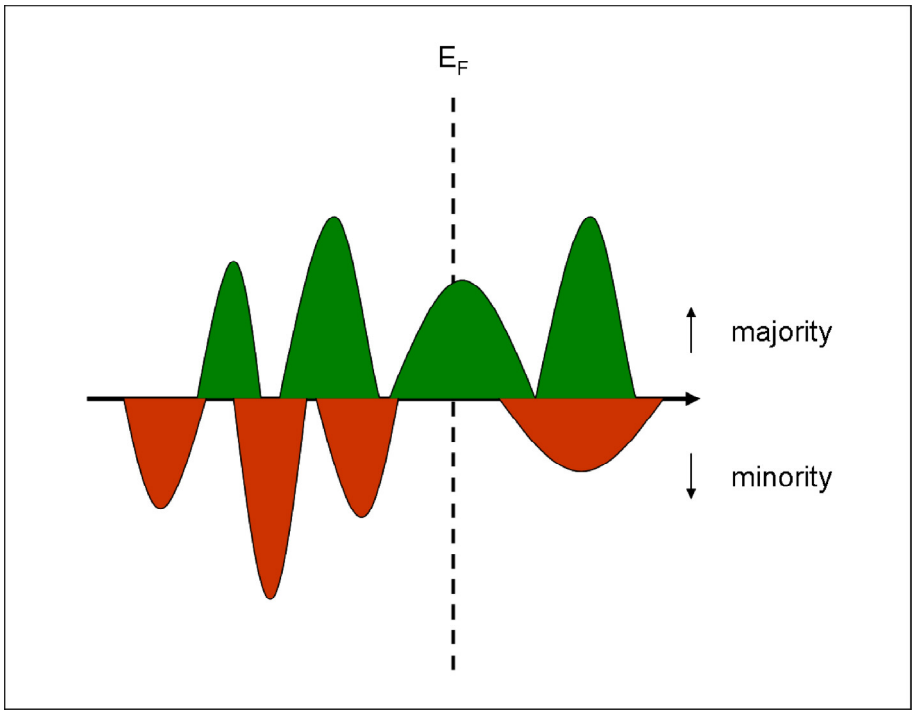

Figure 7.1: Schematic bandstructure of a half metallic ferromagnet.

7.2 Computational Details

The electronic structure of the pure compounds was calculated by means of the full potential linearized augmented plane wave (FLAPW) method as implemented in WIEN2k provided by Blaha *et al.* [103, 104]. The exchange-correlation functional was taken within the generalized gradient approximation (GGA) in the parameterization of Perdew *et al.* [105]. A $25 \times 25 \times 25$ point mesh was used as base for the integration in the cubic systems resulting in 455 k-points in the irreducible wedge of the Brillouin zone. The energy convergence criterion was set to 10^{-5} Ry and simultaneously the criterion for charge convergence to $10^{-3}e^{-}$. The muffin tin radii were set to 2.5 a_{0B} ($a_{0B} = 0.5291772$ Å) for the transition metals as well as the main group element. For the calculation of the transport parameters a modification of the BoltzTraP package was used, which is provided by Madsen and Singh [106]. The Boltzmann transport equations allow to calculate the electrical conductivity from the electronic structure [107, 108, 106]. The matrix of the transport coefficient (σ/τ) of the electrical conductivity is given in the relaxation time approximation by the integral:

$$\sigma_{ij} = -e^2 \int_0^{\infty} \tau_k \, v_i(k) v_j(k) \, \rho(E) \frac{\partial f(E,\mu,T)}{\partial E} \, dE, \tag{7.1}$$

where e is the electron charge, $\rho(E)$ is the density of states, μ is the chemical potential

and $f(E, \mu, T)$ is the Fermi-Dirac distribution. In metals, the chemical potential μ corresponds to the ground state Fermi energy ϵ_F in a good approximation (note: $\mu(T = 0) = \epsilon_F$). The group velocities $v_\alpha(k)$ are given by the derivatives of the band dispersion $v_\alpha(k) = \frac{1}{\hbar}\frac{\partial E_k}{\partial k_\alpha}$. The relaxation time $\tau = \tau_k$ depends on both, the band index as well as the k vector direction. However, detailed studies of the k-dependence of τ have shown that, to a good approximation, τ does not dependend on the direction [109]. In isotropic systems, likewise cubic crystals, only the diagonal terms $\sigma_{ii} = \sigma$ exist.

Similar to the electric conductivity, the electronic thermal transport properties are calculated from the ab-initio electronic structure making use of the Boltzmann transport equations [107, 108, 106]. The electronic part of the thermal conductivity is found from the integral:

$$\kappa^0_{ij} = -\frac{1}{T}\int_0^\infty \tau_k \, v_i(k) v_j(k) \, \rho(E) \, (E-\mu)^2 \, \frac{\partial f(E,\mu,T)}{\partial E} \, dE. \tag{7.2}$$

The Seebeck coefficient is derived from $S_{ij} = [\sigma_{ij}]^{-1}\nu_{ij}$ where (note that the electron charge e is negative):

$$\nu_{ij} = -\frac{e}{T}\int_0^\infty \tau_k \, v_i(k) v_j(k) \, \rho(E) \, (E-\mu) \, \frac{\partial f(E,\mu,T)}{\partial E} \, dE. \tag{7.3}$$

The thermal and electric conductivity integrals contain the relaxation time τ, which is identical in both cases. S does therefore not dependent on the relaxation time if assuming that τ is independent of the electron momentum k or energy. Along with the Seebeck coefficient, the electronic thermal conductivity at zero electric current is defined in an isotropic system as: $\kappa^e = \kappa^0 - T\nu S$. S is small in the material investigated here and κ^c is dominated by κ^0 wherefore the second term will be omitted in the following.

The temperature dependence of the chemical potential $\mu(T)$ of a metal is approximately given by:

$$\mu(T) = \epsilon_F - \frac{\pi^2}{6}(k_B T)^2 \left[\frac{\frac{d\rho(E)}{dE}}{\rho(E)}\right]_{E=\epsilon_F}. \tag{7.4}$$

Due to the condition of charge neutrality the shift of μ is given by $\delta\mu = \mu(T) - \epsilon_F$, which means that the number of thermally created holes below ϵ_F has to be identical with the number of thermally excited electrons above ϵ_F.

7.3 Results and Discussion

7.3.1 First principles calculations

The basis for the calculation of the thermoelectric properties are the band structures. Out of these the transport properties can be calculated. The electronic structure has

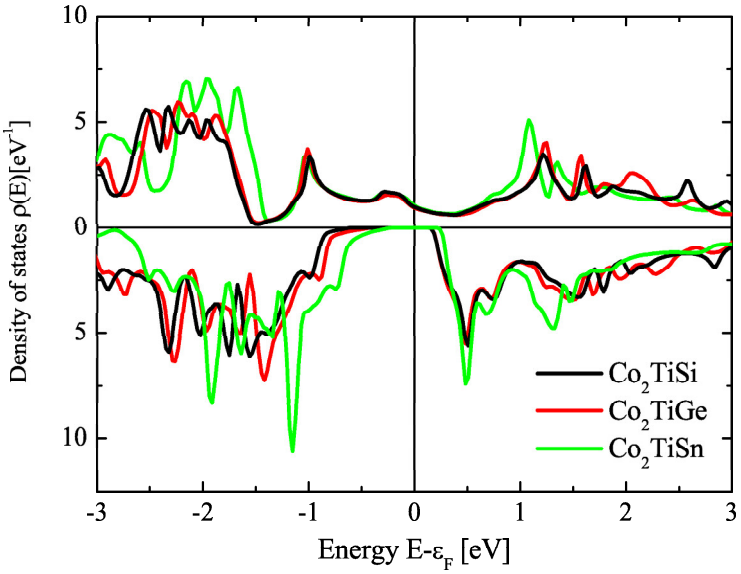

Figure 7.2: Spin polarized density of states for the compounds Co_2TiZ (Z = Si, Ge, Sn). The upper part represents the majority channel and the lower part the minority channel.

been calculated for Co_2TiZ (Z = Si, Ge, Sn) using the fully relativistic, spin polarized Korringa-Kohn-Rostocker (KKR) method [110, 111]. The calculated spinpolarized density of states (DOS) for the compounds is shown in Figure 7.2. As already shown [112], Co_2TiSn is predicted to be a halfmetallic ferromagnet. The same is true for Co_2TiSi and Co_2TiGe. For the majority electrons the DOS diagrams of Co_2TiZ show metallic behavior. The DOS does not change significantly at the Fermi energy with the variation of the Z atom for the majority electrons. All three compounds show a semiconducting band gap for the minority electrons, that decreases with the size of Z.

The calculated optical energy gaps are displayed in table 7.1. The band structures have been calculated with an additional correlation potential U. For all compounds the band gap size decreases with heavier homologues at the Z position with and without U. The results with U show a wider gap and the decrease of its size is less than the ones calculated without U. The results of the band structure calculations with an additional potential U did not improve the description of the band structure and therefore it was neglected in the further investigations. For the calculations with the BoltzTrap package we considered only the spin polarized and the non polarized cases. The resulting densities of states(DOS) close to E_F are displayed in Figure 7.3 from -1 eV to +1 eV. The display range was focused on E_F due to the very narrow distribution of the Fermi-Dirac distribution in the investigated temperature range. Hence only electronic states close to E_F contribute to the conductivity. The DOS is highly increased for

Table 7.1: Band structure parameters for Co_2TiZ Given are the optical band gaps ΔE calculated with and without an additional correlation potential U.

compound	ΔE [eV]	ΔE_U [eV]
Co_2TiSi	0.768500	1.197470
Co_2TiGe	0.569269	1.101640
Co_2TiSn	0.473230	1.041640

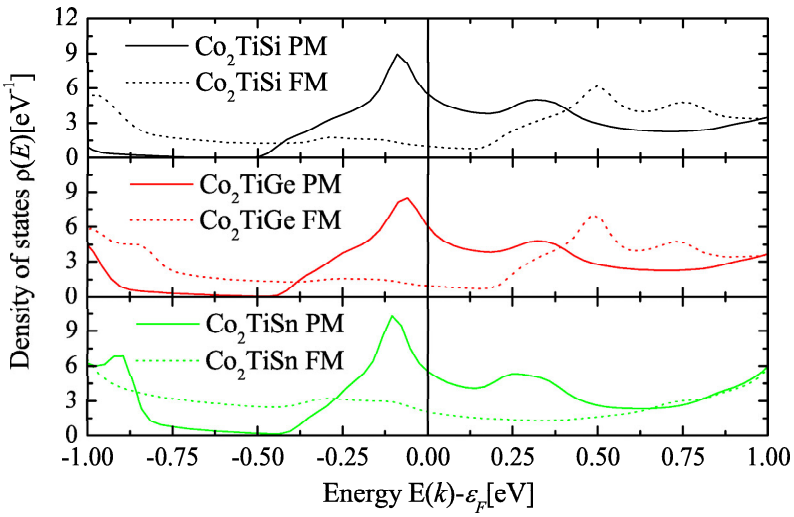

Figure 7.3: Calculated density of states for Co_2TiZ. Displayed are the results for a paramagnetic and a ferromagnetic calculation.

the paramagnetic calculations for all three compounds. Therefore, different transport properties are expected. The DOS for Co_2TiSn close to the Fermi energy is higher than for Co_2TiSi and Co_2TiGe, which is due to the localized d electrons of Sn. The DOS shows no significant derivations at the Fermi energy nor in the range that is relevant for thermally excited electrons. The influence of the bandstructure on the transport properties is discussed in the respective chapter.

The band structure was calculated for all three compounds with and without an additional correlation potential U.

7.3.2 Valence band photoemission spectroscopy

High energy valence band photoemission spectroscopy was performed to support the results of the band structure calculations. Figure 7.4 displays the valence band photoemission spectra and the calculated total density of states of the three compounds investigated here. For better comparison, the density of states is convoluted by a

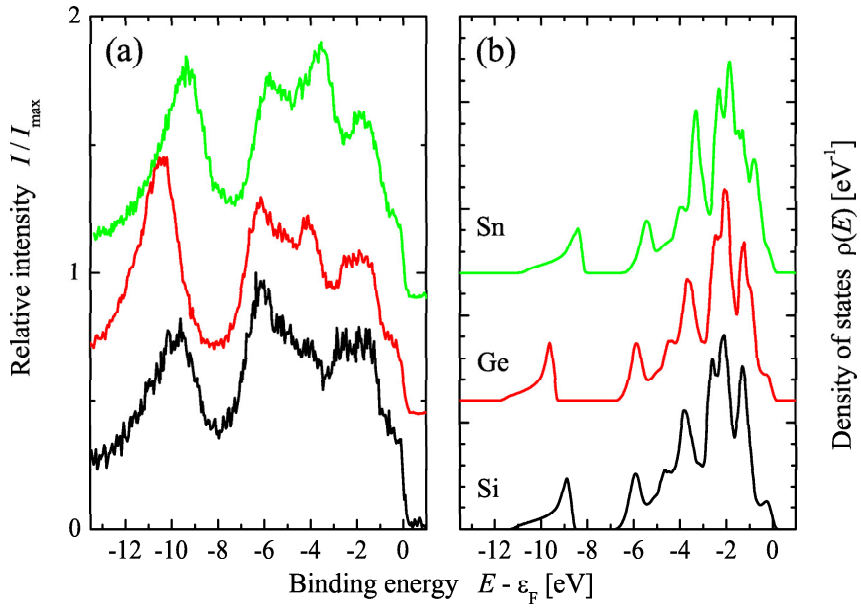

Figure 7.4: Photoemission and density of states of Co_2TiZ (Z=Si, Ge, Sn). (a) shows the valence band spectra and (b) the calculated density of states. The measurements were performed at $T = 300$ K. The density of states is convoluted by a Fermi-Dirac distribution and smoothed by Gaussians to reflect the finite temperature and resolution of the photoemission experiment.

Fermi-Dirac distribution ($T = 300$ K) and smoothed by Gaussian with a width of 250 meV. The latter accounts for the experimental resolution but neglects, however, any broadening caused by lifetime effects. The photoemission spectra were taken at room temperature using an excitation energy of about 6 keV. It was previously demonstrated that the cross section of the contributing states (s, p, and d) are nearly equal at this photon energy [113]. This allows an easy direct comparison of the photoelectron spectra and the calculated density of states. The measured values agree well with the calculated ones and therefore are a good basis for the calculation of the transport properties. Though, one should keep in mind, that the measurements are spin integrated and therefore only the comparison to the total DOS is viable. For a comparison of the spin resolved calculations spin resolved measurements are needed. Such an experimental setup is planned for future investigations.

7.3.3 Structural properties

The structural properties were determined by XRD measurements of the compounds. The results are shown in Figure 7.5.

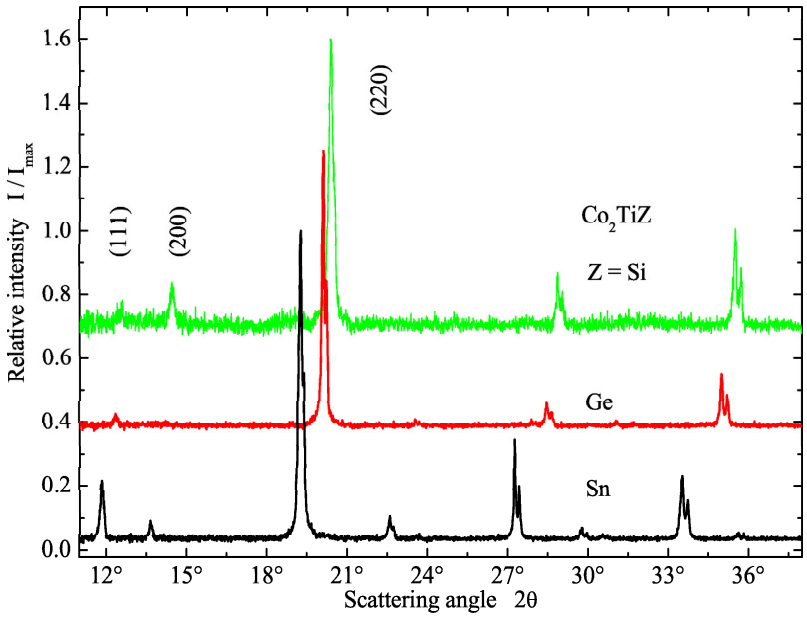

Figure 7.5: XRD for the Co_2TiZ series

No impurity phases were detected. The cell parameters were determined by refinement of the pattern and found to be in excellent agreement with literature except for Co_2TiGe that is still in good agreement with literature. The results are compiled in Table 7.2.

Table 7.2: Lattice parameters of Co_2TiZ. Compared are experimentally determined lattice parameters(a_{exp}) of the compounds Co_2TiSi, Co_2TiGe, and Co_2TiSn with the values from a structural optimization using Wien2k(a_{relax}) and the corresponding values from literature(a_{lit}).

[H] compound	a_{exp}[Å]	a_{relax}[Å]	a_{lit}[Å]
Co_2TiSi	5.733	5.758	5.743 [114]
Co_2TiGe	5.751	5.850	5.831 [41]
Co_2TiSn	6.055	6.093	6.076 [115]

7.3.4 Surface properties

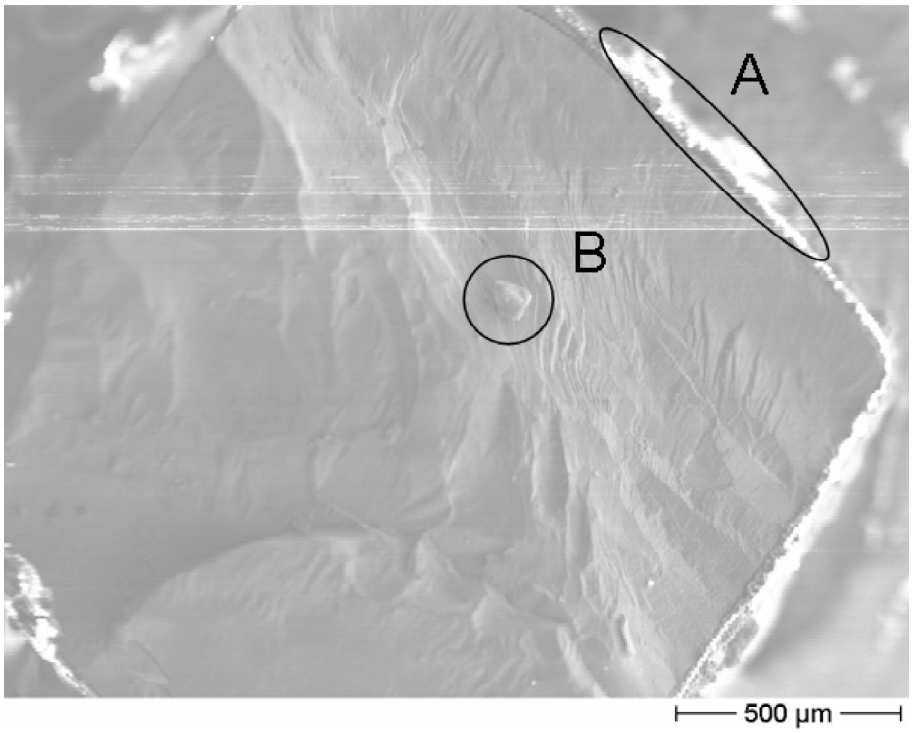

Figure 7.6: SEM micrograph of Co_2TiSi. A and B mark the Al and the Si impurites, respectively.

The energy dispersive X-ray(EDX) spectroscopy was used to indicate the homogeneity of the compounds. This is crucial to the thermoelectric properties, since small segregations can have a huge impact. For the investigation the whole sample surface was included. The results of the quantitative chemical analysis are compiled in Table 7.3. All compositions are within the experimental [116] error of 5 %. On the edges of the samples small Al impurities were found, which emerge from the saw blade, that was used for the cutting. This is shown by the ellipsoid A in the upper right corner. The surfaces are homogeneous, except for Co_2TiSi, which contains small impurities of Si. This is displayed in Figure 7.6. The circle denoted with B marks the aggregation of Si.

Table 7.3: Chemical composition of the Co_2TiZ compounds. Values are given in atomic % with an error range of 5% [116].

Compound	Co_2TiSi	Co_2TiGe	Co_2TiSn
Co	48.41	49.54	53.54
Ti	23.24	23.21	24.69
Z	28.35	27.25	21.43

7.3.5 Magnetic properties

Prior to the thermoelectric properties the magnetic properties were examined. The magnetic properties are very important in the case of Co_2TiZ, because the band structure is influenced strongly by the magnetism. Therefore the Curie temperature (T_c) and the magnetic moment have been determined. The Co_2-based Heusler alloys that are half-metallic ferromagnets show a Slater-Pauling like behavior for the magnetization. The saturation magnetization scales linearly with the number of valence electrons [101, 102] of the compounds. This results in a theoretical magnetic moment of 2 μ_B per formula unit at T=0 K for all three compounds.

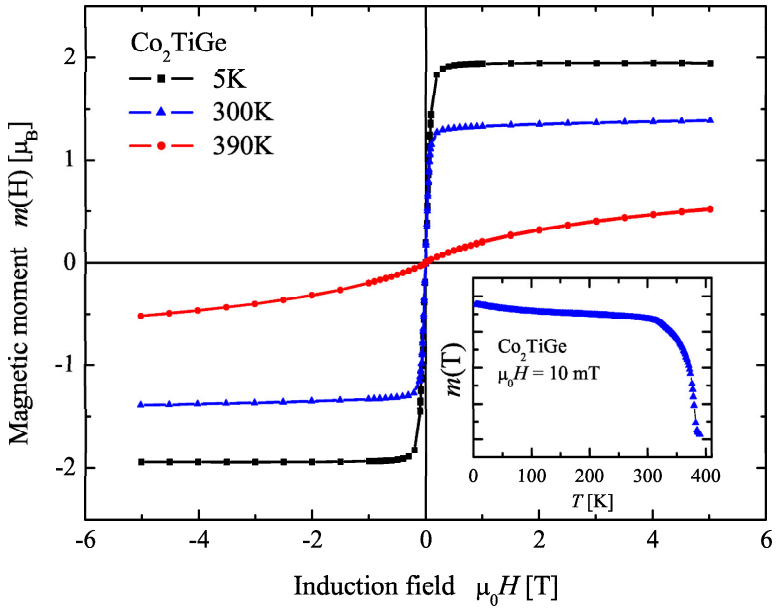

Figure 7.7: Magnetization of Co_2TiGe.
Displayed are the hysteresis curves for T= 5K, 300K, and 390K. The inset shows the temperature dependence measured in an induction field of $\mu_0 H = 10mT$.

Low temperature magnetometry has been carried out by means of the SQUID to investigate the temperature dependence of the magnetisation and to determine the Curie temperatures of the samples. Selected results are shown in Figure 7.7. The total magnetic moments of the ferromagnetic samples, measured at 5 K and in saturation, are just below $2\mu_B$ for all three compounds (see Table 7.4).

The Curie temperatures T_C were determined by the temperature dependence of the magnetisation measured in an induction field of $\mu_0 H = 10mT$. See the inset of Figure 7.7 for an example. The Curie temperatures are 380 K for both Co_2TiSi and Co_2TiGe, and 355 K for Co_2TiSn.

Table 7.4: Experimental and calculational determinations of the Curie temperatures and the total magnetic moments M for the Co_2TiZ compounds.

Compound	T_M[K]	T_{Res}[K]	$M_{SQUID}[\mu_B]$
Co_2TiSi	380±5	370±20	1.96
Co_2TiGe	380±5	350±30	1.94
Co_2TiSn	355±5	360±15	1.97

Kübler [117]developed an ab initio method for calculating the Curie temperatures of an itinerant-electron ferromagnet and applied it to Co_2 based Heusler compounds [118]. The calculated results are in very good agreement with the ones that were obtained in this report.

The values fit the theoretical predictions for the T_Cs of Heusler compounds very well. An approximately linear dependence is obtained for Co_2-based Heusler compounds when plotting the Curie temperature (T_C) of the known, 3d metal based Heusler compounds as a function of their magnetic moment [102]. According to this plot a T_C between 300 K and 400 K is expected.

In Table 7.4 the results of the methods are listed that have been used to determine the Curie temperatures and the magnetic moments. We find an agreement for the determination of the T_c for both the SQUID and the resistivity measurements. The linear dependence [102], which yields values between 350 K and 400 K agrees with experimentally determined values and can be used as a rule of thumb to predict the Curie temperature. The total spin magnetic moments that were experimentally determined by the SQUID agree very well with the given linear dependence. The Slater Pauling rule can be used as a rule of thumb and supports the experimental and calculational findings. The magnetic moment of Co_2TiSn is the one closest to the expected value of $2\mu_B$. It is followed by Si and the Ge.

7.3.6 Transport properties

Electrical resistivity

The resistivity data from 2 K to 400 K were obtained by a standard AC 4 point method and the data from 350 K to 950 K were measured by a standard dc four point method. In Figure 7.8 the resistivity curves of Co_2TiZ (Z= Si, Ge, Sn) are shown as a function of the temperature. The resistivity behaves metallic for all compounds in the low temperature range from 2 K to the respective Curie temperature. At T_c a metal to semiconductor like transition is observed. From there the resistivity declines to around 550 K and stays nearly constant at higher temperatures.

At the Curie temperature a ferromagnetic to paramagnetic transition occurs. In the case of Co_2TiZ this transition is accompanied by a strong change in the resistivity.

Table 7.5: Listing of the residual resistivity ratios RRR of Co_2TiSi, Co_2TiGe, and Co_2TiSn.

Compound	RRR
Co_2TiSi	1.22
Co_2TiGe	1.11
Co_2TiSn	1.40

Therefore, the Curie temperatures can be estimated from the maxima of the resistivities. In Table 7.4 the determined values for the Curie temperature are displayed. The values determined by the resistivity measurements are in reasonable agreement with the ones determined by the magnetometry experiments.

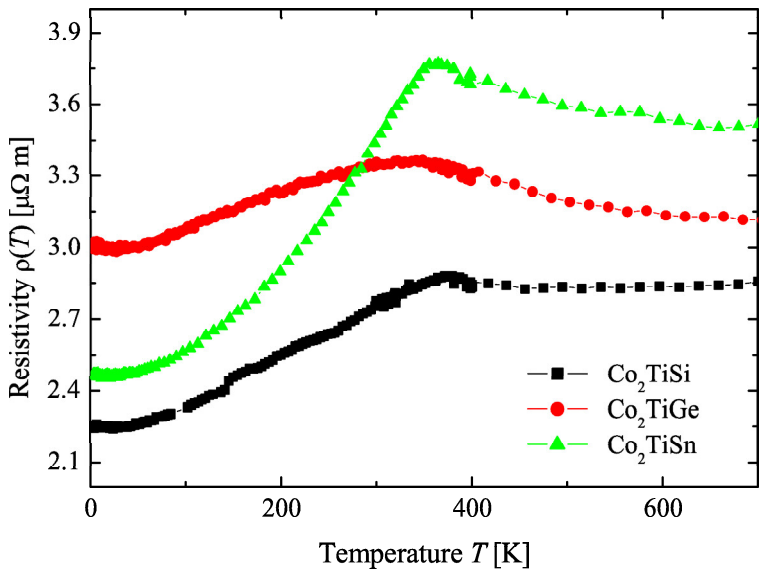

Figure 7.8: Measured temperature dependent electrical resistivity of Co_2TiSi, Co_2TiGe, and Co_2TiSn

The residual resistivity ratios (RRR) were determined for Co_2TiSi, Co_2TiGe and Co_2TiSn, and are summarized in Table 7.5. The values corroborate the assumption, that the Sn containing compound is the best ordered one. The resistivity measurements and the determination of T_c for Co_2TiSn agree well with the findings of Majumdar et al [119].

The decrease of resistivity when reaching T_c is associated to a ferromagnetic- paramagnetic transition. The calculations of the resistivity divided by a scattering factor τ are displayed in Figure 7.9.

The calculations have been carried out in the temperature range from 5 K to 500 K

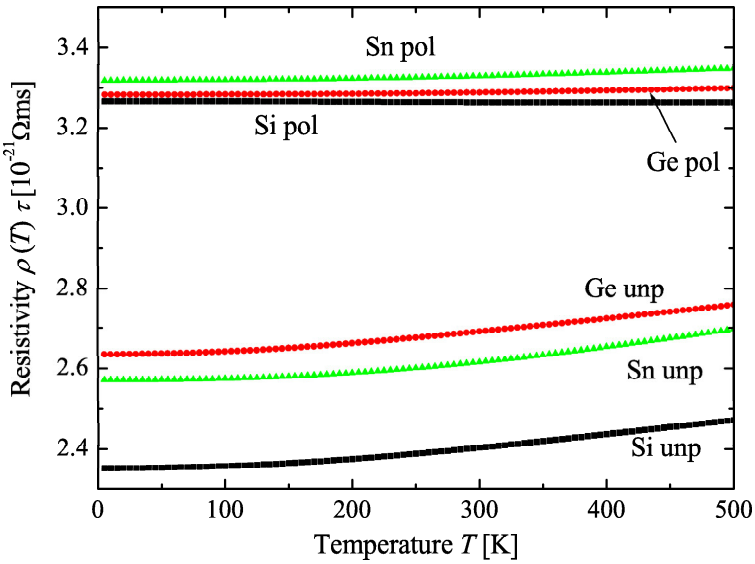

Figure 7.9: Calculated temperature dependent resistivity of Co_2TiSi, Co_2TiGe, and Co_2TiSn

for spin polarized and non spin polarized models. For the spin polarized calculations the resistivity is dominated by the majority electrons. Even at elevated temperatures of 500 K the contribution of the minority electrons to the conductivity is less than 1%. For all compounds the resistivity is metallic, although the spin polarized calculation of Co_2TiSi shows nearly constant resistivity behavior. The resistivities of the non polarized calculations compared to the polarized ones are significantly reduced for all three compounds. Reason for this is the huge change in the band structure that comes along when changing from the polarized to the non polarized model. In Figure 7.10 the resistivity behavior of the compounds for a mixed magnetization is shown. The mixing has been weighted according to

$$S(M) = \frac{M\nu_{FM}/\tau_{FM} + (1-M)\nu_{PM}/\tau_{PM}}{M\sigma_{FM}/\tau_{FM} + (1-M)\sigma_{PM}/\tau_{PM}}, \tag{7.5}$$

where the assignment of the T dependence of M, τ, S, and σ is omitted for simplicity.

The results are shown in Figure 7.10 for Co_2TiGe. Displayed is the resistivity for a spin polarized and a non polarized calculation and a mixture of the two. The weighting has been calculated according to a normalization of the magnetization at 5 K, which is assumed to be 100% at this temperature. For low temperatures the ferromagnetic behavior is dominating the resistivity and then it is sharply declining at the Curie temperature. For temperatures above the Curie temperature, the resistivity behavior

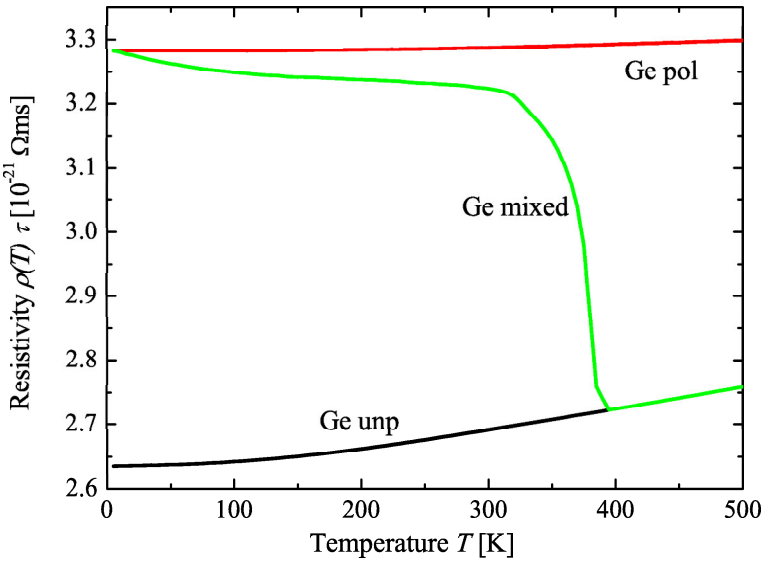

Figure 7.10: Calculated temperature dependent resistivity of Co_2TiGe

is analogous to the non polarized calculation. A drop of about 25% of the resisitivity is observed at the Curie temperature. This explains the experimentally oberved resistivity drop at the Curie temperatures very well, although the drop is not as sharp as expected.

Seebeck coefficient

The Seebeck coefficient was measured from 2 K to 950 K. The determined values are displayed in Figure 7.11. The values are decreasing with higher temperatures down to minimum values of -31μVK^{-1}, -35μVK^{-1}, and -51μVK^{-1} for Co_2TiSi, Co_2TiGe, and Co_2TiSn, respectively at the respective Curie temperatures. From there on the Seebeck coefficients are quite constant and vary little with increasing temperature. This phenomenon is related to the ferromagnetic to paramagnetic transition occurring at the Curie temperature. For all compounds the Seebeck coefficient is negative in the whole temperature range.

The density of states is slightly increasing in the ferromagnetic case whereas it is decreasing in the paramagnetic case which leads to opposite signs for the Seebeck coefficient for both cases.

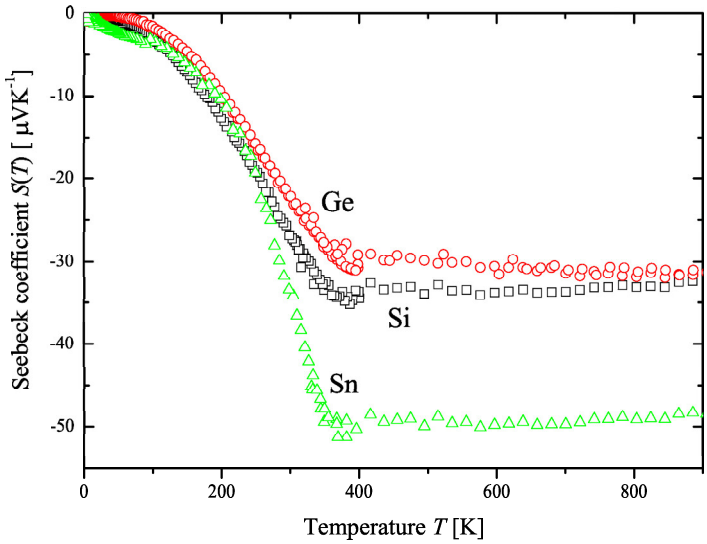

Figure 7.11: Measured temperature dependent Seebeck coefficient of Co_2TiSi, Co_2TiGe, and Co_2TiSn

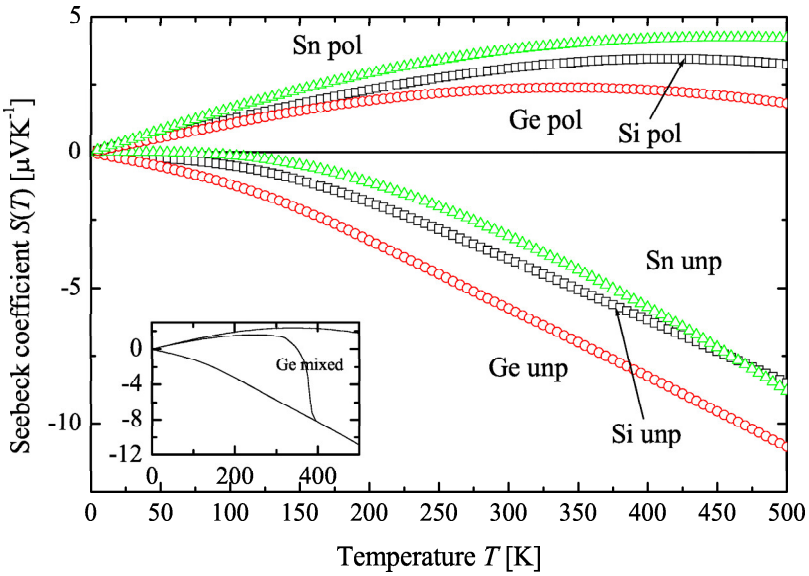

Figure 7.12: Calculated temperature dependent Seebeck coefficient. Shown are the results for Co_2TiSi, Co_2TiGe, and Co_2TiSn for each spin direction.

The Seebeck coefficient comprises whether electrons or holes are created with increasing temperature. As it is independent of the relaxation time it provides a sensitive test of the electronic structure for metals in the vicinity of the Fermi energy. The experi-

mentally determined Seebeck coefficient is clearly negative at $T > 50$ K. This cannot be explained by the spin polarized electronic structure. It is dominated by the majority electrons, even if a mixing with the minority states is assumed at $T > 0$. For a better description the polarized and the non polarized results have to be weighted again, like it was done for the resistivity. In Figure 7.12 the Seebeck coefficient is calculated in the temperature range from 5 K to 500 K for the paramagnetic and the ferromagnetic ground state. For the ferromagnetic calculation the Seebeck coefficient is positive in the whole temperature range for all three compounds. Opposing to that all paramagnetic calculations reveal negative values. The values for the Seebeck coefficient are too small, even if a total non polarization is assumed. The increase of the Seebeck coefficient can be explained with additional scattering at grain boundaries or impurities of the sample, which are not accounted for by the calculations. Even after the weighting the absolute values do not agree well, but the general behavior of the Seebeck coefficient can now be explained.

Thermal conductivity

For the further evaluation of the compounds as possible thermoelectric materials thermal conductivity measurements were performed in the range from 2 K to 400 K.

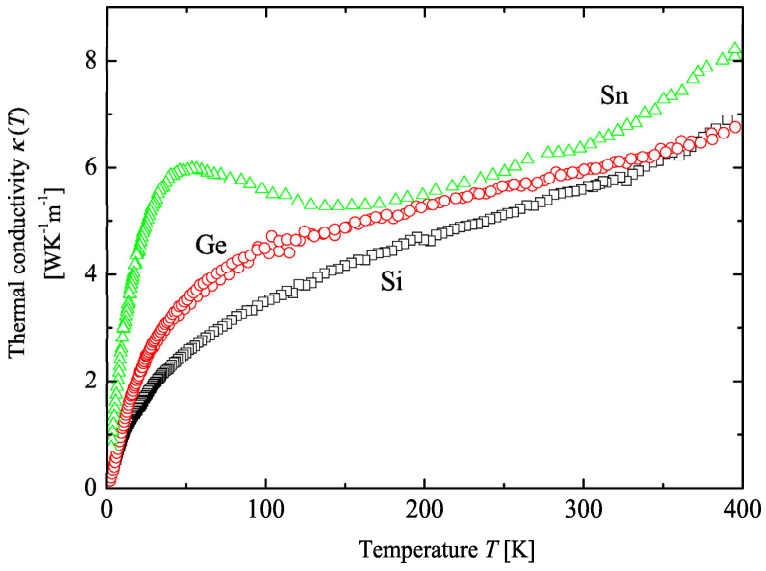

Figure 7.13: Measured temperature dependent thermal conductivity of Co_2TiSi, Co_2TiGe, and Co_2TiSn

In Figure 7.13 the thermal conductivities of the studied samples are displayed. For Co_2TiSi and Co_2TiGe the thermal conductivity is increasing with the T^3 law at low

temperatures and then changing to a linear increase with T. Co_2TiSn follows the T^3 law too but reaches a maximum at about 50 K. From there the thermal conductivity decreases to the temperature of 140 K. Afterwards the thermal conductivity linearly increases like it is observed for the other compounds. This behavior has been reported in literature before [120, 56, 17, 121, 122].

At low temperatures, when κ is limited by boundary scattering, κ increases steadily with increasing temperature, reaches its peak at approximately 50 K and then decreases above 50 K, when the phonon-phonon scattering is expected to dominate. The peak indicates that the Co_2TiSn sample is very well ordered and has few point defects. The more disordered the crystal is, the more the low temperature peak is discriminated. The thermal conductivity can be described as $\kappa=\kappa_e+\kappa_l$. κ_e is the electronic contribution and κ_l is the lattice contribution. Figure 7.14 displays the experimental and the calculated results of the electronic part of the thermal conductivity κ_e.

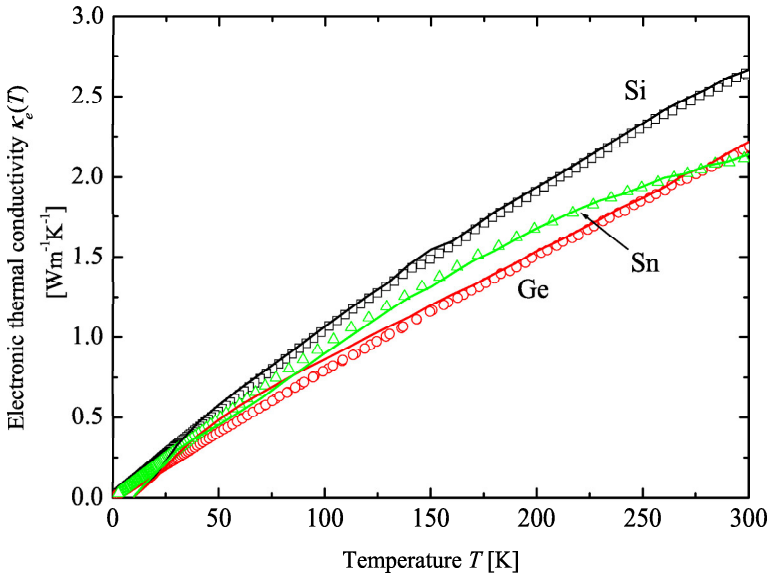

Figure 7.14: Calculated temperature dependent electronic thermal conductivity of Co_2TiSi, Co_2TiGe, and Co_2TiSn divided by a scattering factor. Symbols represent values determined by resistivity measurements and the lines indicate the calculated results.

The experimental results are derived from the resistivity via the Wiedemann-Franz law. The theoretical data are results of the calculation with the BoltzTrap package. The electrons of the minority channel were neglected due to their small contribution in this temperature range. The scattering factor has been determined by comparison of the experimental and calculated results of the resistivity. The agreement of the values is very good for all three compounds. We calculated $\kappa_e+\kappa_l$ and received ratios of κ_e/κ_l

1.03, 0.73, and 0.74 for Co_2TiSi, Co_2TiGe, and Co_2TiSn respectively at 300 K. This ratio needs further optimization to achieve 0.5 which is proposed [52] to be the best ratio for $\kappa_e+\kappa_l$ with respect to the figure of merit.

In Figure 7.15 the thermal conductivity and its electron and phonon dependent part are shown. It can be easily seen, that the phonon part is constant above 100 K. Further increases of κ_{tot} are only related to the electronic contribution. Since the changes in resistivity are small, the dependence is mainly dependent on the temperature. This explains the linear increase of the experimentally determined values. At 390 K a small change in the electronic part of the thermal conductivity is observed. This is again related to the ferromagnetic to paramagnetic transition, which results in a change of the resistivity and therefore a change in the thermal conductivity.

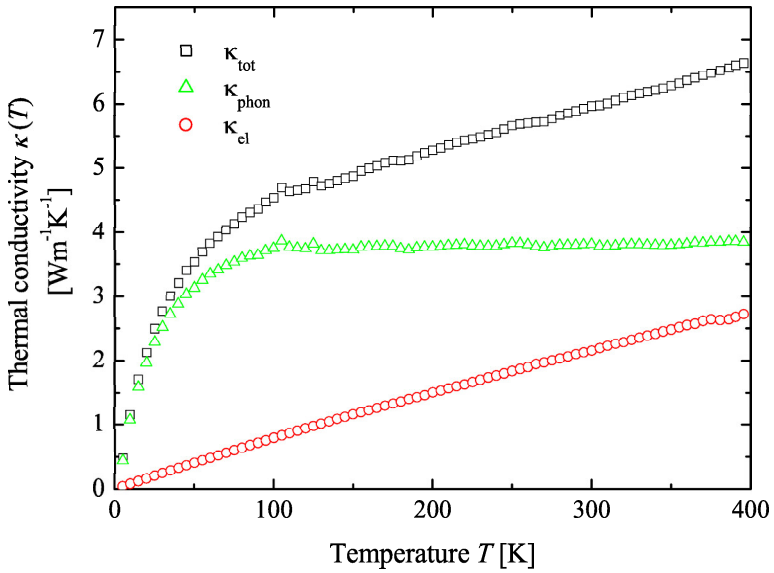

Figure 7.15: Thermal conductivity of Co_2TiGe. Displayed are the total thermal conductivity κ_{tot}, the phononic part κ_{phon}, and the electronic part of the thermal conductivity κ_e.

7.4 Summary and Conclusion

The Co_2TiZ (Z = Si, Ge, Sn) compounds were investigated theoretically and experimentally. Band structure calculations predict halfmetallic ferromagnetism for all three compounds. The results of the valence band photoemission spectroscopy confirm the calculational results of the spin polarized and the non polarized band structure calculations. The Boltzmann transport theory was used to predict transport properties up to temperatures of 500 K. The Curie temperature and the magnetic moment were deter-

mined by experimental and theoretical methods. The theoretical results are close to the experimental ones, especially for the linear dependency of the Curie temperature to the valence electrons and the Slater Pauling rule. Further EDX and XRD measurements were used to confirm the phase purity and homogeneity of the samples. Only small impurities were found. All compounds show a metallic like resistivity for low temperatures up to their Curie temperature. From there on they change to semiconducting like behavior. This behavior is attributed to a ferromagnetic to paramagnetic transition, that strongly influences the band structure. The Seebeck coefficients are all negative and reach their maximum values at their respective Curie temperatures. The highest value achieved is -52 $\mu VK^{-1}m^{-1}$ for Co_2TiSn. The calculated findings of the Seebeck coefficient agree with the experimentally gained ones concerning the trend. The thermal conductivity was measured and divided into the electronic and the phononic part. The electronic part of the compounds was calculated and it was found to be in good agreement with the experimentally obtained values. The thermal conductivity values of $\approx$5 $WK^{-1}m^{-1}$ are comparable to the ones found for other Heusler compounds [123]. The highest value for the figure of merit in the temperature range from 2 K to 400 K was at 400 K for Co_2TiSn with a ZT of 0.05. Further optimization of the figure of merit can be achieved by controlled doping of the compounds, usage of nanoparticles [52], or improvement of the crystal structure by appropriate heat treatment.

8 Summary and Outlook

8.1 Summary

In this work $C1_b$ and $L2_1$ Heusler compounds have been investigated on their structural and thermoelectric properties. It was tried to enhance the figure of merit of the investigated compounds. Several approaches for the enhancement were applied. The various approaches can be reduced to two concepts. The first is the optimization of the carrier concentration. In this concept the concentration of the charge carriers is adjusted by the substitution of atoms in the compounds with atoms of unequal valence electron counts. The percentage of the substituted atoms is varied until a maximum for the Power factor is reached. The second concept is the reduction of the thermal conductivity. The reduction of the thermal conductivity can be achieved by variation of the the grain size, mass fluctuation scattering, impurities, and the rattling effect of loosely bound atoms. The results of the applied concepts are shown in the respective chapters. Further new materials were investigated.

In chapter 3 the measurement results for the $TiCo_{1-x}(Fe_{0.5}Ni_{0.5})_{1-x}Sb$ series are presented. Co was substituted by equal amounts of Ni and Fe to introduce additional mass fluctuation scattering. Small increases of the Seebeck coefficient were achieved for the compositions $TiCo_{0.6}(Fe_{0.2}Ni_{0.2})Sb$ and $TiCo_{0.8}(Fe_{0.1}Ni_{0.1})Sb$. The resistivities were not reduced significantly, but the metal to semiconductor transition observed for TiCoSb vanished. The substituted compounds show semiconducting behavior. Further the high temperature stability and the thermal conductivity were successfully improved.

In chapter 4 the properties of the series $TiCo_xNi_{1-x}Sn_{1-x}Sb_x$ are described. Aim of the simultaneous substitution of Co by Ni and Sb by Sn was to introduce additional mass fluctuation scattering. As a result the Seebeck coefficient was reduced for increasing values of x. The reduction of the resistivity compensated the decrease of the Seebeck coefficient and therefore the Power factor was enhanced. The very low values of down to 2 $Wm^{-1}K^{-1}$ at 400 K for the thermal conductivity boosted the ZT values. Up to date, the found values are among the smallest ones that have been observed for $C1_b$ compounds. The reduction of the thermal conductivity is based on Ti rich microstrures, that were observed by SEM micrographs. As a result the investigated compounds show ZT values, that are in the order of magnitude of state of the art materials.

In chapter 5 the thermoelectric properties of the compounds LiAlSi, LiAlGe, and LiGaSi are presented. In this chapter the approach of the introduction of rattling atoms into a cage-like structure was successfully applied. The thermal conductivity of

the compounds was successfully reduced for the LiAlGe and LiGaSi compounds. In these compounds the rattling Li ions scatter the phonons effectively and reduce the thermal conductivity. The achieved values for the Seebeck coefficient are in the range of 100-140 μVK^{-1} at 400 K. All compounds show metallic resistivity behaviour with values in the range of 4-45 μ Ω m. The constituents of the compounds are abundant in the earth crust, cheap, and nontoxic. This makes them perfect candidates for an industrial use in thermoelectric devices.

In chapter 6 several substitutions were tried to increase the figure of merit for TiCoSb based compounds. In the series $TiCo_{1+x}Sb$ the amount of Co was varied and its influence on the thermoelectric properties was investigated. The addition of Co to the compound significantly reduced the thermal conductivity with nearly retaining the properties of the Seebeck coefficient and the electrical resistivity. Further investigations on the structure have to be performed to reproduce the achieved values. In the series $TiCo_{1-y}Cu_ySb$ Co was substituted by Cu to optimize the Power factor. The decrease of the Seebeck coefficient was compensated by the decrease in resistivity and the figure of merit remained nearly unchanged. Therefore the substitution of Co by Cu seems not to be suitable to enhance the Power factor. Finally, in the series $TiCoSb_{1-z}Bi_zSb$ was substituted by Bi. The substitution of Sb by Bi lead to a decrease of the resistivity and an increase of the Seebeck coefficient while the thermal conductivity remained nearly unchanged. With a reduction of the thermal conductivity the TiCoSb compound substituted with Bi becomes very attractive for thermoelectric applications. The compound is estimated to have $ZT \approx 1$. This is equivalent to state of the art thermoelectric materials.

In chapter 7 the compounds Co_2TiZ were investigated theoretically and the experimentally. The application of electronic band structure calculations in combination with the BoltzTrap code were demonstrated on the class of half-metallic ferromagnets. It was shown that with band structure calculations and the BoltzTrap package the transport properties of complicated electronic band structures can be predicted. The determined values for the Seebeck coefficient are comparably small to other thermoelectric materials, but this disadvantage is compensated by their low resistivity. Remarkable is, that the Seebeck coefficient and the resistivity show anomalous behavior above the respective Curie temperatures of the compounds. Metal to semiconductor like transitions at the Curie temperature and a constant Seebeck coefficient above the Curie temperature are observed. The behavior seems to be unique at least to the best of my knowledge.

8.2 Outlook

The decisive point in the research in the field of thermoelectrics is still the figure of merit at an appropriate temperature. Only materials that possess $ZT \geq 1$ will have

a chance to be successfully utilized in large scale. The compounds investigated in this study show ways to significantly enhance the thermoelectric properties of the known compounds. With the application of the improvements shown in this thesis a figure of merit of 1 is in reach. Although, a figure of merit of 1 or higher has not been achieved yet.

In chapter 3 the stabilization of TiCoSb with Ni and Fe was demonstrated. The substitution of Co by Ni and Fe can be applied to other TiCoSb based compounds to extend the chemical stability to higher temperatures. The improved chemical stability and the reduction of the thermal conductivity will both be valuable improvements for TiCoSb based thermoelectric materials.

In chapter 4 the series $TiCo_xNi_{1-x}Sn_{1-x}Sb_x$ and the influence of micro structures on the thermal conductivity were investigated. The extraordinary low thermal conductivity that has been achieved for $Ni_{0.9}Co_{0.1}TiSn_{0.9}Sb_{0.1}$ needs further investigation. An understanding of this very low value is very important for the further exploration in the field of thermoelectrics. A deeper insight of this phenomenon can be achieved by the theoretical investigation of the phononic properties. The phononic properties can be calculated based on the results of electronic band structure calculations with the PHONON software, written by Parlinski. The code has been successfully applied to describe phonon spectra of several compounds [124, 125]. A reduction of the thermal conductivity like it was shown here with a preservation of the high Power factor of Heusler compounds will be a major breakthrough in thermoelectric research.

In chapter 5 the Li containing compounds were investigated. LiAlSi showed the best values for Seebeck coefficient and resistivity, but had a quite high thermal conductivity. The thermal conductivity was significantly reduced for LiAlGe. The series $LiAlSi_{1-x}Ge_x$ is expected to have superior thermoelectric properties compared to LiAlSi and LiAlGe. The introduction of Li atoms in structures with big holes is supposed to reduce the thermal conductivity. The introduction of the Li atoms into the compounds can be achieved using the Zintl concept. The series $TiNiSn_{1-x}In_xLi_x$ is expected to show a lowered thermal conductivity. x has to be chosen in a way, that the mass fraction of Li is above 5% and the Power factor remains high. Additionally the AlLiSi system is considered as a material for Li ion batteries and as a hydrogen storage material [126].

In chapter 6 several compounds based on TiCoSb are described. For the series $TiCo_{1+x}Sb$ the concentration x has to be found for the optimized ZT value. This can be achieved by choosing smaller stepsizes for x. For the series $TiCoSb_zBi_{1-z}$ the stepsize of z has to be reduced as well. Further a systematic investigation of the evaporation of Sb and Bi have to be performed. A combination of the results from chapter 3 and chapter 6 resulting in the compound $TiCo_{0.6}Ni_{0.2}Fe_{0.2}Sb_{0.95}Bi_{0.05}$ is expected to yield an improvement for ZT.

In chapter 7 the series Co_2TiZ was theoretically and experimentally investigated.

The calculations could reproduce the experimentally obtained values qualitatively. For a quantitative description or even prediction of the properties, the scattering factor τ has to be included into the calculations. If τ can be included the electronic properties can be described. In combination with the prediction of the phononic properties by the PHONON code, the thermoelectric properties of the materials can be predicted. A combination of the two programs yields a powerful tool for the characterization of thermoelectric materials. The experimental values that were found for the series have to be investigated further. Especially magnetic investigations should help in understanding the observed behavior. It is not yet clear, why the Seebeck coefficient and the resistivity show the anomaly at the Curie temperature. A possible application for the anomalous behaviour of the Seebeck coefficient is to make a thermo element composed of Co_2TiSi and Co_2TiSn. Due to the constant difference of the Seebeck coefficient between Co_2TiSi and Co_2TiSn above their Curie temperatures no additional calibration is necessary.

The control of the stoichiometry of the TiCoSb based compounds is of great importance. In most publications the low temperature resistivity measurements of TiCoSb show a metal to semiconductor transition. Although in a few articles a strictly semiconducting behaviour for pure TiCoSb is reported [127, 34]. Since non stoichiometric amounts of Sb are supposed to cause the metal to semiconductor transition several series where synthesized with varying amounts of Sb. The compound of the composition $TiCo_{0.93}Sb_{1.03}$ showed remarkable properties. The properties are displayed in Figure 8.1. The Seebeck coefficient is increased to $-500\mu VK^{-1}$ and the resistivity is increased to 1000 $\mu\Omega m$ at 300 K. The resistivity behaviour is not semiconducting over the full measurement range but the metal to semiconductor transition has been moved to about 80 K. A lower temperature for the metal to semiconductor transition indicates less impurities. A further reduction of the impurities is necessary to understand how TiCoSb compounds can be optimized.

It was suggested by Hicks and Dresselhaus [128] that a reduction of the particle size can enhance the figure of merit. Several attempts in this direction have successfully been applied [13]. This approach can also be applied to the Heusler compounds. In collaboration with G. Jakob it is planned to synthesize thin films of several Half Heusler compounds like TiNiSn, TiPtSn and ZrNiSn [6, 120, 129] and use them as model systems for the investigation of their thermoelectric properties. When a high enough figure of merit is reached and the material is usable under economical and ecological aspects, a thermoelectric generator can be built. The use of thermoelectric generators can help to reduce the consumption of fossil fuels and make machines more energy efficient. This leads to a reduction of the CO_2 emission and to a cooling of exhaust gases. A reduction of the CO_2 emission might have a slowing effect on the global warming [130, 131]. Exhaust gases are supposed to be one of the origins of the 'Urban

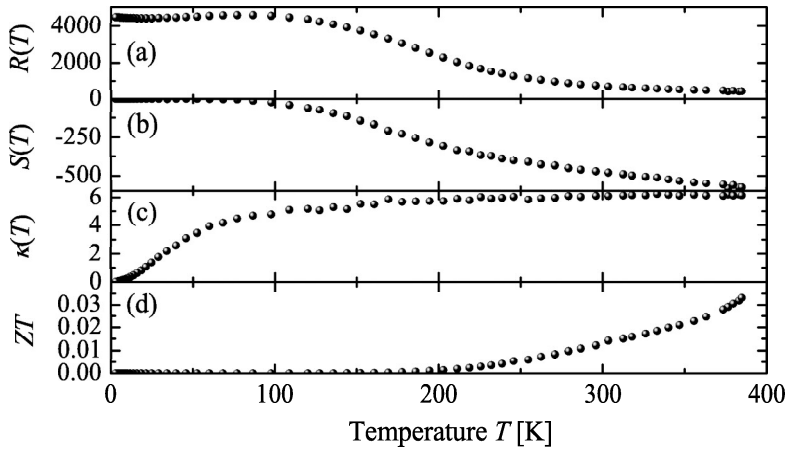

Figure 8.1: Thermoelectric properties for nominal $TiCo_{0.93}Sb_{1.03}$. Shown are (a) the resistivity $R(T)$, (b) the Seebeck coefficient $S(T)$, (c) the thermal conductivity $\kappa(T)$, and the dimensionless figure of merit ZT.

Heat Island' effect [132]. This effect will be reduced with cooler exhaust gases of cars. The field of use for thermoelectric materials is widespread, but applications in power plants and automobiles seem to be the most attractive for an industrial utilization. The increasing demand of power and the consumption of the remaining fossil fuels lead to a shortage of energy. Thermoelectric materials may solve our future needs for energy or at least they may prolong the time, where fossil fuels can be used as resources.

9 Abstract

9.1 Abstract

Abstract of the Dissertation of J. Barth

Heusler Compounds as thermoelectric materials

December 1, 2009

This work reports on new Heusler compounds and their thermoelectric properties. Several new compounds were successfully synthesized and their resistivity, Seebeck coefficient, thermal conductivity, and the figure of merit were determined. At the beginning a short introduction to the physical description of the thermoelectric properties is given. In the main part several series of new Heusler compounds and their thermoelectric properties are shown. Finally a conclusion of summary and an outlook will be given, that demonstrate future possibilities of the investigated compounds.

In the series $TiNi_{1-x}Co_xSn_{1-x}Sb_x$ Ni was substituted with Co and Sn with Sb. Especially for high Ni concentrations the figure of merit was enhanced compared to unsubstituted TiCoSb. This enhancement is based on the strong reduction of the thermal conductivity. The found values are among the lowest, that have been determined up to date for Heusler compounds.

In the series $TiCo_{1-x}(Fe_{0.5};Ni_{0.5})_{0.5}Sb$ Co was substituted with Ni and Fe in equal shares. This substitution lead to a stabilization of the compound and to a reduced loss of Sb during the synthesis. This resulted in an increase of the Seebeck coefficient and to an improved thermal stability.

Furhter Li containing Heusler compounds were investigated and their thermoelectric properties were determined. The so called "rattling" approach was successfully applied and yielded large reductions of the thermal conductivity of the compounds. The Li atoms were viewed as the rattlers and the rest of the structure as the cage. The application was only successful, when the cages were of a sufficient size.

The material class of half metallic ferromagnets as a new materialclass was investigated as well. We used the 26 valence electron compounds Co_2TiSi, Co_2TiGe, and Co_2TiSn as model systems. At first the transport properties were determined theoretically with the Wien2k code and a modified BoltzTrap code. Then the properties were measured and compared to the calculated ones. The predictions of the Seebeck coefficient were in good agreement with the measured values for moderate temperatures. The electronic part of the thermal conductivity was in excellent agreement with the experimentally determined ones. Only the resistivity was afflicted with large uncertainties, due to the absence of the scattering factor.

In the final chapter several substitutions of TiCoSb are illustrated. The amount of Co was varied and it had a huge influence on the thermoelectric properties of the compounds. The Seebeck coefficient could be increased and the thermal conductivity reduced at the same time. In another series Co wsa substituted with Cu, but no significant enhancement of the power factor could be observed. The decrease in resistivity was compensated by the decrease of the Seebeck coefficient. In another attempt Sb was substituted with Bi. In this case a good improvement

of the figure of merit could be achieved, due to an increase of the Seebeck coefficient and a parallel decrease of the resistivity.

List of Figures

List of Tables

Bibliography

[1] G. J. Snyder and E. S. Toberer. *Nature materials*, 7:105–114, 2008.

[2] T. M. Tritt. *Science*, 283:804, 1999.

[3] D.M. Rowe. *CRC Handbook of Thermoelectrics*. CRC, Boca, Raton, 1995.

[4] F.D. Rosi. *Solid-State Electron.*, 11:833, 1968.

[5] C. B. Vining. *CRC Handbook of Thermoelectrics*. CRC, Boca, Raton, 1995.

[6] N. Shutoh and S. Sakurada. *J. Alloys Comp.*, 389:204–208, 2005.

[7] T. C. Harmann, P.J. Taylor, M.P. Walsh, and B.E. LaForge. *Science*, 297:2229, 2000.

[8] S. Ogut and K.M. Rabe. *Phys. Rev. B*, 51:10443, 1995.

[9] K. Fujita, T. Mochida, and K. Nakamura. *Jpn. J. Appl. Phys.*, 40:4644–4647, 2001.

[10] B.C. Sales, B.C. Chakoumakos, D. Mandrus, and J.W. Sharp. *J. Solid State Chem.*, 146:528–532, 1999.

[11] D-Y Chung, T. Hogan, P. Brazis, M. Rocci-Lane, C. Kannewurf, M. Bastea, C. Uher, and M. Kanatzidis. *Science*, 287:1024–1027, 2000.

[12] K. F. Hsu, S. Loo, F. Guo, W. Chen, J. S. Dyck, C. Uher, T. Hogan, E. K. Polychroniadis, and M. Kanatzidis. *Science*, 303:818–821, 200+4.

[13] R. Venkatasubramanian, E. Siivola, T. Colpitts, and B. O'Quinn. *Nature*, 413:597–602, 2001.

[14] H. C. Kandpal, C. Felser, and R. Seshadri. *J. Phys. D: Appl. Phys.*, 39:776, 2006.

[15] D. Jung, H.-J. Koo, and M.-H. Whangbo. *J. Mol. Struc. (THEOCHEM)*, 527:113–119, 2000.

[16] S. Sakurada and S. Shutoh. *Appl. Phys. Lett.*, 86:2105, 2005.

[17] H. Hohl, A. P. Ramirez, C. Goldmann, G. Ernst, B. Woelfing, and E. Bucher. *J. Phys.: Condens. Matter*, 11:1697, 1999.

[18] Q. Shen, L. Zhang, L. Chen, T. Goto, and T. Hirai. *J. Mater. Sci. Lett.*, 20:2197, 2001.

[19] Y. Kimura, T. Kuji, A. Zama, Y. Shibata, and Y. Mishima. *Solid-State Ionics*, 2006.

[20] F. Heusler. *Verh. Dtsch. Phys. Ges.*, 1903.

[21] F. Heusler, W. Starck, and E. Haupt. *Verh. Dtsch. Phys. Ges.*, 1903.

[22] A. J. Bradley and J. W. Rodgers. *Proc. Royal Soc. A*, 144:340–359, 1934.

[23] S. J. Poon. *Recent Trends in Thermoelectric Materials Research I.* Academic, New York, 2001.

[24] S. Bhattacharya, M. J. Skove, M. Russell, T.M. Tritt, Y. Xia, V. Ponnambalam, S.J. Poons, and N. Thadhani. *Phys. Rev. B*, 77:184203, 2008.

[25] http://www1.eere.energy.gov/vehiclesandfuels/pdfs/deer_2004/session4/2004_deer_fairbanks2.pdf.

[26] C. M. Bhandari and D. M. Rowe. *CRC Handbook of Thermoelectrics.* CRC, Boca, Raton, 1995.

[27] H. J. Goldsmid. *Applications of Thermoelectricity.* Methuen Monograph, London, 1960.

[28] C.S. Lue and Y.-K. Kuo. *Phys. Rev. B*, 66:085121, 2002.

[29] E. Müller, C. Stiewe, D.M. Rowe, and S.G.K. Williams. *Thermoelectrics Handbook Macro To Nano.* CRC, Boca, Raton, 2006.

[30] Quantum Design. *Physical Property Measurement System Thermal Transport Option User's Manual.* Quantum Design, USA, San Diego, 2002.

[31] T. Wu, W. Jian, X. Li, Y. Zhou, and L. Chen. *J. Appl. Phys.*, 102:1037051–1037055, 2007.

[32] M. Zhou, L. Chen, C. Feng, D. Wang, and J.F. Li. *J. Appl. Phys.*, 101:1137141–1137146, 2007.

[33] J. Tobola, S. Kaprzyk, R. V. Skolozdra, and M. A. Kouacou. *J. Phys.: Condens. Matter*, 10:1013, 1998.

[34] B. Balke, G. H. Fecher, A. Gloskovskii, J. Barth, K. Kroth, C. Felser, R. Robert, and A. Weidenkaff. *Phys. Rev. B*, 77:045209, 2008.

[35] J. O. Sofo and G. D. Mahan. *Phys. Rev. B*, 49:4565–4570, 1994.

[36] R. Chasmar and R. Stratton. *J. of Electron. Control*, 7:52, 1959.

[37] G. D. Mahan. *J. Appl. Phys.*, 65:1578, 1989.

[38] T. Sekimoto, K. Kurosaki, H. Muta, and S. Yamanaka. *J. All. and Comp.*, 394:122–125, 2005.

[39] Yu. Stadnyka, V. A. Romaka, M. Shelyapina, Yu. Gorelenko, L. Romaka, D. Fruchart, A. Tkachuk, and V. Chekurin. *J. All. Comp.*, 421:19–23, 2006.

[40] J. Tobola, L. Jodin, P. Pecheur, and H. Scherrer. *Phys. Rev. B*, 64:155103–1–7, 2001.

[41] P. J. Webster and K.R.A. Ziebeck. *J. Phys. Chem. Solids*, 34:1647–1654, 1973.

[42] A. Szytula, Z. Tomkowicz, and M. Turowski. *Act. Phys. Pol., A*, 44:147–149, 1973.

[43] L. Vegard. *Zeitschr. f. Phys. A Hadr. and Nucl.*, 5:17–26, 1921.

[44] N. Tareuchi, K. Gosho, M. Hiroi, and M. Kawakami. *Phys. B: Cond. Mat.*, 359-361:1183–1185, 2005.

[45] Y. Xia, V. Ponnambalam, S. Bhattacharya, A. L. Pope, S. J. Poon, and T. M. Tritt. *J.Phys.: Condens. Matter*, 13:7789, 2001.

[46] A. Kjekshus, P.G. Peterzens, T. Rakke, and A.F. Andresen. *Phase Transition*, 38:469–480, 1992.

[47] A. Kjekshus, T. Rakke, and A.F. Andresen. *Phase Transition*, 38:127–220, 1992.

[48] H. Holseth and A. Kjekshus. *Act. Chem. Scan.*, 23:3043–3050, 1968.

[49] T. Rosenqvist. *Acta Metall.*, 1:761–763, 1953.

[50] I.V. Chumak, V.V. Pavlyuk, G.S. Dmytriv, and J. Stepien-Damm. *J. All. Comp.*, 307:223–225, 2000.

[51] C.M. Bhandari and R.M. Rowe. *Thermal conduction in semiconductors.* Wiley Eastern Limited, New Delhi, India, 1988.

[52] C. M. Bhandari. *CRC Handbook of Thermoelectrics.* CRC, Boca, Raton, 1995.

[53] T. Katayama, S. W. Kim, and Y. Kimura. *J. Electron. Mat.*, 32:1758–1763, 2003.

[54] S. Bhattacharya, M. J. Skove, M. Russell, T. M. Tritt, Y. Xia, V. Ponnambalam, S. J. Poon, and N. Thadhani. *Phys. Rev. B*, 77:184203, 2008.

[55] K. Takahiro, W. W. Kim, K. Yoshisato, and M. Yoshinao. *J. Electron. Mat.*, 32:1160–1165, 2003.

[56] C. Uher, J. Yang, and S. Hu. *Phys. Rev. B*, 59:8615, 1999.

[57] L. Chaput, J. Tobola, P. Pecheur, and H. Scherrer. *Phys. Rev. B*, 73:045121, 2006.

[58] M. Zhou, C. Feng, L. Chen, and X. Huang. *J. Alloy. Comp.*, 391:194–197, 2005.

[59] S. R. Culp, J. W. Simonson, S. J. Poon, V. Ponnambalam, J. Edwards, and T. M. Tritt. *Appl. Phys. Lett.*, 93:022105, 2008.

[60] J. Pierre, R. V. Skolozdra, Yu. Gorelenko, and M. Kouacou. *Journ. of Magn. and Magn. Mat.*, 134:95–105, 1994.

[61] J. H. N. van Vucht, H. A. C. M. Bruning, H. C. Donkersloot, and A. H. Gomes de Mesquita. *Phil. Res. Rep.*, 19:407–421, 1964.

[62] P. Pietrowsky and P. Duwez. *Journ. of Metals*, 3:772–772, 1951.

[63] R. Marazza, R. Ferro, and G. Rambaldi. *Journ. of Less Com. Met.*, 39:341–345, 1975.

[64] J. Pierre, R.V. Skolozdra, and Y. V. Stadnyk. *J. Magn. Magn. Mater.*, 128:93, 1993.

[65] T. Katayama, S. W. Kim, Y. Kimura, and Y. Mishima. *J. Electron. Mat.*, 32:1160–1165, 2003.

[66] S. Kuroiwa, H. Kawashima, H. Kinoshita, H. Okabe, and J. Aikimitsu. *Phys. C*, 466:11–15, 2007.

[67] J. Yang, D. T. Morelli, G. P. Meisner, W. Chen, S. J. Dyck, and C. Uher. *Phys. Rev. B*, 67:165207, 2003.

[68] M. S. Dresselhaus, G. Chen, M. Y. Tang, R. Yang, H. Lee, D. Wang, Z. Ren, J.-P. Fleurial, and P. Gogna. *Adv. Mater.*, 19:1043–1053, 2007.

[69] C. Wood. *Rep. Prog. Phys.*, 51:459, 1988.

[70] D. M. Rowe. *J. Power Sources*, 19:247, 1987.

[71] G. A. Slack and M. A. Hussain. *J. Appl. Phys.*, 70:2694, 1991.

[72] H.J. Goldsmid. *Thermoelectric Refrigeration.* Pion Ltd., London, 1986.

[73] U. Birkholz and G.Z. Haacke. *Z. Naturforsch.*, 161:5, 1962.

[74] R. R. Ainsworth and W.W. Scanlon. *Phys. Rev.*, 111:1029, 1958.

[75] G.S. Nolas, G. A. Slack, D.T. Morelli, T. M. Tritt, and A. C. Ehrlich. *J. Appl. Phys.*, 79:4002–4008, 1996.

[76] E. H. Zintl and G. Brauer. *Z. Phys. Chem. Abt. B*, 20:245, 1933.

[77] H. Nowotny and K. Bachmayer. *Mh. Chem.*, 80:734, 1949.

[78] R. Juza and F. Hund. *Z. Anorg. Chem.*, 257:1, 1948.

[79] O. K. Andersen. *Phys. Rev. B*, 12:3060, 1975.

[80] L. Spina, Y.-Z. Jia, M.B. Ducourant, M. Tillard, and C. Belin. *Zeitschr. f. Krist.*, 218:740–746, 2003.

[81] H. Nowotny and F. Holub. *Monatsh. f. Chem.*, 91:877–887, 1960.

[82] H.U. Schuster, H.W. Hinterkeuser, W. Schaefer, and G. Will. *Acta Cryst. C*, 61:i51–i53, 2005.

[83] E. Bockelmann and H.U. Schuster. *Z. f. Naturf., Teil B Anorg. Chem., Org. Chem.*, 24:1189–1189, 1969.

[84] W. Bockelmann and H.U. Schuster. *Z. f. Anorg. u. Allg. Chem.*, 410:241–250, 1974.

[85] W. Bockelmann, H. Jacobs, and H. U. Schuster. *Z. Anorg. Allg. Chem.*, 410:233, 1974.

[86] N. E. Christensen. *Phys. Rev. B*, 32:6490–6497, 1985.

[87] Y. Miura, M. Shirai, and K. Nagao. *J. Appl. Phys.*, 99:08J112, 2006.

[88] W.-J. Xie, X.-F. Tang, and Q.-J. Zhang. *Chin. Phys.*, 16:3549–3552, 2007.

[89] K. Kishimoto and T. Koyanagi. *J. of All. and Comp.*, 463:89–91, 2008.

[90] F. Casper, C. Felser, R. Seshadri, C. P. Sebastian, and R. Pöttgen. *J. Phys. D: Appl. Phys.*, 41:35002, 2008.

[91] B.C. Sales, D. Mandrus, and R.K. Williams. *Science*, 272:1325, 1996.

[92] K. Kroth, B. Balke, G.H. Fecher, V. Ksenofontov, C. Felser, and H.-J. Lin. *Appl. Phys. Let.*, 89:202509, 2006.

[93] M. A. S. Boff, G. L. F. Fraga, D. E. Brandão, and A. A. Gomes. *Phys. status solidi*, 139:67, 1993.

[94] T. Stopa, J. Tobola, and S. Kaprzyk. *Intern. conf. on thermoelec.*, 25:132–135, 2006.

[95] D. R. Lide. *CRC Handbook of Chemistry and Physics.* CRC Press, Boca Raton, Florida, 84th edition edition, 2003.

[96] T. Wu, W. Jiang, X. Li, Y Zhou, and L. Chen. *J. Appl. Phys.*, 102:103705, 2007.

[97] W. Ting, W. Jiang, X. Lia, S. Baia, S. Liufu, and L. Chen. *J. Alloy. Comp.*, 467:590–594, 2009.

[98] L. L. Wang, L. Miao, Z. Y. Wang, W. Wei, R. Xiong, H. J. Liu, J. Shi, and X. F. Tang. *J. Appl. Phys.*, 105:013709, 2009.

[99] R. A. de Groot, F. M. Müller, P. G. van Engen, and K. H. J. Buschow. *Phys. Rev. Lett.*, 50:2024, 1983.

[100] J. Kübler, A. R. Williams, and C. B. Sommers. *Phys. Rev. B*, 28:1745, 1983.

[101] I. Galanakis, P. H. Dederichs, and N. Papanikolaou. *Phys. Rev. B*, 66:174429, 2002.

[102] G. H. Fecher, H. C. Kandpal, S. Wurmehl, and C. Felser. *J. Appl. Phys.*, 99:08J106, 2006.

[103] P. Blaha, K. Schwarz, P. Sorantin, and S.B. Tricky. *Comput. Phys. Commun.*, 59:399, 1990.

[104] P. Blaha, K. Schwarz, G. K. H. Madsen, D. Kvasnicka, and J. Luitz. *WIEN2k, An Augmented Plane Wave + Local Orbitals Program for Calculating Crystal Properties.* Karlheinz Schwarz, Techn. Universitaet Wien, Wien, Austria, 2001.

[105] J. P. Perdew, K. Burke, and M. Ernzerhof. *Phys. Rev. Lett.*, 77:3865, 1996.

[106] G. K. H. Madsen and D. J. Singh. *Comput. Phys. Commun.*, 175:67–71, 2006.

[107] W. Jones and N. H. March. Wiley Interscience, London, 1973.

[108] U. Mizutani. Cambridge University Press, Cambridge, 2001.

[109] W. W. Schulz, B. P. Allen, and N. Trivedi. *Phys. Rev. B*, 45:10886, 1992.

[110] J. Korringa. *Physica*, 13:392, 1947.

[111] W. Kohn and N. Rostoker. *Phys. Rev.*, 94:1111, 1954.

[112] M. C Hickey, A. Husmann, S.N Holmes, and G.A.C. Jones. *J. Phys.: Condens. Matter*, 18:2897–2903, 2006.

[113] G. H. Fecher, B. Balke, A. Glsokowskii, S. Ouardi, C. Felser, T. Ishikawa, M. Yamamoto, Y. Yamashita, H. Yoshikawa, S. Ueda, and K. Kobayashi. *Appl. Phys. Let.*, 92:193513, 2008.

[114] K.H.J. Buschow, P.G. van Engen, and R. Jongebreur. *J. Magn. Magn. Mater.*, 38:1–22, 1983.

[115] P.G. van Engen, K.H.J. Buschow, and M. Erman. *J. Magn. Magn. Mater.*, 30:374–382, 1983.

[116] P. F. Schmidt. *Praxis der Rasterelektronenmikroskopie und Mikrobereichsanalyse.* Expert Verlag, Renningen, Germany, 1994.

[117] J. Kübler. *J. Phys.: Condens. Matter*, 18:9795 – 9807, 2006.

[118] J. Kübler, G. H. Fecher, and C. Felser. *Phys. Rev. B*, 76:024414, 2007.

[119] S. Majumdar, M. K. Chattopadhyay, V.K. Sharma, K.J.S. Sokhey, S.B. Roy, and P. Chaddah. *Phys. Rev. B*, 72:012417, 2005.

[120] Q. Shen, L. Chen, T. Goto, T. Hirai, J. Yanga, G. P. Meisner, and C. Uher. *Appl. Phys. Let.*, 79:4165–4167, 2001.

[121] Y. Xia, S. Bhattacharya, V. Ponnambalam, A. L. Pope, S. J. Poon, and T. M. Tritt. *J. Appl. Phys.*, 88:1952, 2002.

[122] S. Bhattacharya, T. M. Tritt, Y. Xia, V. Ponnambalam, S. J. Poon, and T. N. Thadhani. *Appl. Phys. Lett.*, 81:43, 2002.

[123] C. S. Lue and Y.-K. Kuo. *Phys. Rev. B*, 66:085121, 2002.

[124] M. M. Koza, M. R. Johnson, R. Viennois, H. Mutka, L. Girard, and D. Ravot. *Nat. Mat.*, 7:805, 2008.

[125] K. Parlinski, Z. Q. Li, and Y. Kawazoe. *Phys. Rev. Lett.*, 78:4063, 1997.

[126] J.-C. Zhao, M. Andrus, J. Cui, Y. Gao, J. Lemmon, T. Raber, J. Rijssenbeek, G. Rubinsztajn, G. Soloveichik, C. Read, and P. Bakke. *FY Annual Progress Report*, DE-FC3605GO15062, 2006.

[127] Yu. Stadnyk, Yu. Gorelenko, A. Tkachuk, A. Goryn, V. Davydov, and O. Bodak. *J. All. Comp.*, 329:37–41, 2001.

[128] L. D. Hicks and M. Dresselhaus. *Phys. Rev. B*, 47:12727–12731, 1993.

[129] A. Horyn, A. Bodak, L. Romaka, Yu. Gorelenko, A. Tkachuk, V. Davydov, and Yu. Stadnyk. *J. All. Comp.*, 363:10–14, 2004.

[130] D. A. Lashof and D. R. Ahuja. *Nature*, 344:529–531, 1990.

[131] R. E. Dickinson and R. J. Cicerone. *Nature*, 319:109–115, 1986.

[132] R. D. Bornstein. *J. of Appl. Meteor.*, 7:575–582, 1968.